Iron-rich Fe-O compounds at Earth's core pressures

Jin Liu^{1,2#*}, Yang Sun^{3#}, Chaojia Lv¹, Feng Zhang⁴, Suyu Fu⁵, Vitali B. Prakapenka⁶, Cai-Zhuang Wang⁴, Kai-Ming Ho⁴, Jung-Fu Lin^{5*}, Renata M. Wentzcovitch^{3,7,8*}

¹Center for High Pressure Science and Technology Advanced Research, Beijing 100094, China

²CAS Center for Excellence in Deep Earth Science, Guangzhou, 510640, China

³Department of Applied Physics and Applied Mathematics, Columbia University, New York, NY 10027, U.S.A.

⁴Department of Physics, Iowa State University, Ames, Iowa 50011, U.S.A.

⁵Department of Geological Sciences, Jackson School of Geosciences, The University of Texas at Austin, Austin, TX 78712, U.S.A.

⁶Center for Advanced Radiation Sources, University of Chicago, Chicago, IL 60439, U.S.A.

⁷Department of Earth and Environmental Sciences, Columbia University, New York, NY 10027, U.S.A.

⁸Lamont–Doherty Earth Observatory, Columbia University, Palisades, NY 10964, U.S.A.

*Equal contribution: J.L. and Y.S.

*Email: afu@jsg.utexas.edu (J.-F.L.), jin.liu@hpstar.ac.cn (J.L.), and rmw2150@columbia.edu (R.M.W.)

Keywords: Earth's core composition | crystal structure prediction | chemical reaction | deep oxygen | layered motifs

Oxygen and iron are the most abundant elements on Earth, and their compounds are key planet-forming components. While oxygen is pervasive in the mantle, its presence in the solid inner core (IC) is still debatable. Yet, this issue is critical to understanding the core-mantle co-evolution and the geomagnetic field generation. Thus far, iron monoxide (FeO) is the only known stoichiometric compound in the Fe–FeO system, and the existence of iron-rich Fe_nO compounds has long been speculated. Here we report that iron reacts with FeO and Fe₂O₃ at 220–260 GPa and 3,000–3,500 K in laser-heated diamond-anvil cells. *Ab initio* structure searches using the adaptive genetic algorithm indicate that a series of stable stoichiometric Fe_nO compounds (with n > 1) can be formed. Like ε -Fe and B8-FeO, Fe_nO compounds have close-packed layered structures featuring oxygen-only single layers separated by iron-only layers. Two solid solution models with compositions close to Fe₂O, the most stable Fe-rich phase identified, explain the x-ray diffraction patterns of the experimental reaction products quenched to room temperature. These results suggest that Fe-rich Fe_nO compounds with close-packed layered motifs might be stable under IC conditions. Future studies of the elastic, rheological, and thermal transport properties of these more anisotropic Fe_nO solids should

provide new insights into the seismic features of the inner core, inner core formation process and composition, and the thermal evolution of the planet.

40 Introduction

The composition and the nature of solid phases in the Earth's core remain largely uncertain. While iron is the major component in Earth's liquid outer core (OC) and solid inner core (IC), seismology requires light elements to account for the IC and OC's "density deficit" relative to pure iron. S, S, Si, C, H, and O are the most likely light elements in the liquid core. Light elements may be incorporated into the solid IC as the OC continuously solidifies by forming iron-rich compounds, such as Fe₇C₃, Fe₃S, and Fe₃Si. High-pressure melting experiments found that eutectic Fe-FeO liquids can contain much oxygen, e.g., 15 wt % at IC boundary conditions. Modeling of core-mantle differentiation also indicates oxygen is a vital light element in the liquid core. The Fe-O system has shown rich stoichiometry under oxygen-rich conditions, e.g., recently discovered FeO₂ under lower-mantle conditions. However, oxygen has been excluded from the IC because of its limited solubility in solid iron observed at low pressures and the absence of known Fe-rich Fe-O compounds. The discovery of stable solid Fe-O alloys at core pressures reported in this paper changes this view, potentially impacting our understanding of the origin of the density deficit contrast between the inner and outer core, outer core composition, inner core formation process, evolution, properties, etc..

Few studies have attempted to identify such O-bearing Fe-rich solids. In particular, *ab initio* studies by Sherman¹³ and Alfè *et al.*¹⁴ addressed substitutional and interstitial Fe_nO structural models that were unstable against decomposition into the end-members Fe and FeO. Weerasinghe *et al.*¹⁵ performed a crystal structure search on the Fe-O system and predicted the possible existence of low-enthalpy iron-rich Fe_nO phases under core pressures. Still, none has yet been synthesized at core pressures. Previous studies have shown that FeO transforms from an insulating inverse-B8 phase to a metal with the NiAs-type (B8) structure at pressures higher than 120 GPa.^{16,17} The latter features alternating single-species (Fe-only or O-only) close-packed layers with layered motifs similar to ε-Fe. Pure oxygen also becomes metallic at 96 GPa.¹⁸ The change of the chemical character of FeO and O at high pressures may change their solubility in solid iron at megabar pressures.¹⁹ Here, we combine high pressure and temperature (*P-T*) experiments and crystal structure predictions to search for iron-rich Fe-O compounds at pressures greater than 200

GPa. Because crystal structure searches identify low-temperature phases, we solve the x-ray diffraction (XRD) patterns of samples produced in *P-T* experiments but quenched to room temperature.

70 71

72

73

74

75

76

77

78

79

80

81

82

83

84

85

86

87

88

89

90

91

92

93

94

95

96

97

98

68

69

Results and Discussion

Experimental synthesis. We performed five high P-T experiments to synthesize Fe_nO compounds. We carried out synchrotron XRD experiments on the Fe-FeO system under high P-T conditions using laser-heated diamond-anvil cells (LHDAC) at the Advanced Photon Source (APS) at Argonne National Laboratory, and Shanghai Synchrotron Radiation Facility (SSRF). Starting materials were mixtures of pure iron with FeO or Fe₂O₃ powder in a size range of submicron to a few microns (refer to details in Methods). Repetitive micro-second laser pulses were employed to heat the sample for a short period of ~1 sec. This laser heating strategy significantly reduced potential carbon diffusion from diamond anvils into the sample chamber (see Supplementary Note 1). Samples were well insulated from the diamond anvils by the KCl pressure-transmitting medium and were heated up evenly on both sides to reach high temperatures readily. No reaction was observed in the first three runs at 100–200 GPa up to 2,600 K (Fig. S1), consistent with previous experimental studies of FeO. 12,20 In run 4, the Fe-FeO mixture was compressed firstly to 220 GPa at room temperature. Upon laser pulse heating to 2,000–3,000 K, diffraction peaks of both ε-Fe and B8-FeO merely became sharper without the appearance of any new reflections. Further laser pulse heating to 3,000–3,200 K showed dramatic XRD pattern changes in a few seconds (left panel in Fig. S2). The integrated diffraction peak intensities of corresponding Fe and FeO phases reduced rapidly, indicating that iron reacted with FeO above 3,000 K and 220–230 GPa. A similarly rapid chemical reaction happened in run 5, starting from a Fe-Fe₂O₃ mixture, compressed to 200-250 GPa at room temperature, and exposed to repetitive laser pulse heating. After reaching ~3,000 K, the peak intensities of the Fe and Fe₂O₃ phases decreased, while a set of additional diffraction peaks emerged (right panel in Fig. S2). At least until 260 GPa and 3,500 K, they remained unaltered before the anvils shattered upon further heating.

The diffraction peaks of the new phases did not change significantly after quenching the sample to room temperature (see Figs. 1 and S2). The quenched new phase(s) remain (meta)stable at room temperature upon decompression to ~160 GPa. To improve the quality of the XRD patterns of the quenched samples, we rotated the DAC by $\pm 10^{\circ}$ around the incident x-ray beam direction.

This procedure significantly improved the XRD peak intensities relative to the background in these polycrystalline samples (Figs. S3 and S4). The short one-second data collection time makes this procedure very challenging at high *P-T*, and the high-temperature XRD patterns show a relatively higher background intensity (Fig. S2). This was another reason for using the XRD patterns collected at room temperature and 220–245 GPa to identify the new phases. The new diffraction peaks from Fe+FeO and Fe+Fe₂O₃ reactions show consistent *d*-spacings (Fig. S5), indicating similar phases are produced under different experimental conditions. The new peaks could not be indexed to high-pressure phases of known oxygen-rich Fe-O compounds (e.g., Fe₄O₅, Fe₅O₆, Fe₅O₇, Fe₂O_{3+δ}, and FeO₂ in Fig. S6), ^{10,21-24} or iron carbides (e.g., Fe₇C₃ and Fe₃C in Fig. S7). ²⁵⁻²⁷

Crystal structure prediction. To solve the XRDs, we first conducted crystal structure searches for Fe_nO (n > 1) compounds using the adaptive genetic algorithms (AGA) at 215 GPa.²⁸ By searching in a wide range of Fe-rich compositions (see details in Methods), several new stoichiometric Fe_nO phases are found to be more stable than the combination of two endmembers, ε -Fe and B8-FeO. Figure 2a shows the convex hull obtained from these crystal structure searches. Four compounds with Fe₃O (space group $P6_3/mmc$), Fe₂O ($P\overline{3}m1$), Fe₃O₂ ($R\overline{3}m$), and Fe₄O₃ ($R\overline{3}m$) stoichiometries are ground states at 215 GPa. The Fe₆O₅ ($R\overline{3}m$) phase is very close to the convex hull with only 0.2 meV/atom above it. All these new Fe-rich compounds have single species (Fe-only or O-only) hexagonal close-packed layers, similar to the endmember phases ε -Fe ($P6_3/mmc$) and B8-FeO ($P6_3/mmc$) (Fig. 2b). Furthermore, most low-enthalpy compounds also have hexagonal close-packed layers, as noted by the red symbol in Fig. 2a.

To study the close-packing motifs in these phases, we select structures whose formation enthalpies are within 26 meV/atom (~300 K) above the convex hull. The lattice parameter *c* of these structures displays nearly linear dependence on the number of layers in the primitive cell (Fig. 2c), suggesting a similar layered motif in all these structures. Examining these structures' stacking sequences, we find a simple compound formation rule. Only seven different three-layer stacking sequences out of twelve possible ones are present in these low-energy structures (see Fig. 2d). The Fe-Fe-Fe layer sequence favors the ABA stacking more than the ABC, consistent with the stacking in ε-Fe. Layer sequences involving oxygen, e.g., Fe-O-Fe or Fe-Fe-O, favor the ABC stacking over the ABA. Five arrangements involving adjacent O-O layers, e.g., Fe-O-O or O-Fe-O with ABA stacking are absent among these structures. Therefore, O-only layers are well

separated from each other. This stacking rule explains why previously proposed Fe_nO models are unstable. ^{13,14} They included oxygen as substitutional and interstitial ions. The BiI₃-type (R-3) model is hexagonal, ¹⁴ but the oxygen layers are not close-packed. All those atomic arrangements have high enthalpy. A previous computational search found an Fe₃O hexagonal structure ($P\bar{6}m2$)¹⁵ more similar to the $P6_3/mmc$ ground state revealed here. However, the enthalpy of the $P\bar{6}m2$ phase is still ~10 meV/atom higher than the $P6_3/mmc$ phase (Fig. S8). Further calculations up to IC pressures confirm the stability of $P6_3/mmc$ Fe₃O against the decomposition into Fe and FeO (Fig. S8). The dynamic stability of these new phases is also confirmed at both 215 GPa and 380 GPa (Fig. S9). High temperatures typical of the IC might introduce anharmonic effects that should be investigated carefully using appropriate methods for high-temperature calculations. ²⁹⁻³¹

XRD solutions. We first compare the predicted XRD patterns of the computationally identified Fe_nO phases with the experimental ones. The four Fe_nO phases in the convex hull can partially match the XRD lines of the quenched reaction products but do not provide a complete interpretation of the diffraction patterns (Fig. S10). By including a few metastable Fe_nO phases, the multi-phase aggregate XRD better matches the experimental data at both 220 GPa and 245 GPa (Fig. S11). Considering that all these Fe_nO phases follow the same basic stacking rule, we anticipate the entropic stabilization of disordered solid solutions at high temperatures. To clarify this point, we set up Reverse Monte Carlo (RMC) simulations of supercell structures with up to 60 layers (~10 nm) to search for the Fe/O stacking sequence that best matches the experimental XRD patterns. The interlayer distances were set using the most probable spacings found in the crystal structures identified with the AGA (see Fig. 3a and refer to Methods for more details of RMC simulations).

The XRD deviation, D_{XRD} , which is the criterion used to select preferred structures during the RMC sampling, is defined as $D_{XRD} = \sqrt{\langle (I_{exp}(2\theta) - I_{sim}(2\theta))^2 \rangle}$, i.e., the mean square deviation between the simulated, I_{sim} , and the experimental, I_{exp} , peak intensities. The 2θ range analyzed is restricted to 9.2–10.2° at 220 GPa and 10.6–11.6° at 245 GPa, corresponding to the prominent peaks of the new reaction products in Fig. 1. Fig. 3b shows D_{XRD} values for different supercell sizes and iron concentrations obtained in RMC simulations. The smallest D_{XRD} at 220 GPa points to a 42-layer structure with chemical composition Fe₂₈O₁₄ shown in Fig. 3c. This structure's XRD matches all additional experimental peaks of reaction products. *Ab initio*

calculations show the formation enthalpy of this phase is only 28 meV/atom above the convex hull. This supercell's calculated equation of state agrees well with the experimental one (see Supplementary Note 2 and Fig. S12), confirming that this structure and composition are a reasonable solution for the experimental XRD. A similar RMC was performed to solve the XRD of the reaction products of Fe and Fe₂O₃ at 245 GPa (Fig. S13). A 38-layer structure solution with composition Fe₂₅O₁₃ can match the experimental data well, as shown in Fig. S3. Analyses of these structural models indicate they represent structures lacking long-range stacking or chemical order. However, they display medium-range structural order (MRO), i.e., domains with preferred stacking order at the scale of ~ 20 atomic layers (~ 30 Å) (see Supplementary Note 3 and Figs. S14-S16). Some short-range-order domains are also observed, e.g., the 5-layer sequence FeOFeOFe appears several times in Figs. S15c,d and S16a,b. The combination of and interference between the MRO domains give rise to the multi-peak patterns in the experimental XRD. The new reaction products likely consist of a disordered alloy with compositional fluctuation in the structure. The rapid temperature quench of these entropically stabilized high-temperature phases retains the disordered nature of the high-temperature phase. The high inner core temperatures may favor the stabilization of these high entropy phases. On the other hand, the long geological time scale may equilibrate an aggregate also containing the stoichiometric Fe_nO phases predicted on the convex hull. The formation of a single disordered phase vs. an aggregate containing the stoichiometric Fe_nO compounds depends on the entropy versus enthalpy competition in Fe_nO which will define the high P-T Fe-FeO phase diagram at relevant conditions.

181

161

162

163

164

165

166

167

168

169

170

171

172

173

174

175

176

177

178

179

180

182

183

184

185

186 187

188

189

190

191

Electronic density of states. Figure 4 shows the electronic density of states (DOS) of ε-Fe, Fe₃O, Fe₂O, and B8-FeO at 215 GPa and $T_{el} = 3,000$ K. All Fe_nO phases discovered are metallic. In ε-Fe, the Fermi level falls on a valley (Fig. 4a), while in B8-FeO, it falls on a peak. Consistently, in Fe_nO the carrier density increases systematically with increasing oxygen content. In Fe₂O, the Fermi level falls on a shallow valley, and the DOS has features resembling those of ε-Fe and FeO. Fe₃O has two kinds of iron: those with (Fe1, Fe2, Fe4, Fe5) and those without (Fe3, Fe6) oxygen first neighbors (see Fig. 4). Fe3-type iron's contribution to the DOS (red area in Fig. 4b) resembles that of ε-Fe, while Fe1-type iron's contribution (blue area in Fig. 4b) resembles Fe₂O's.

The chemical bonding nature in Fe_nO phases is analyzed using electron localization function (ELF) and Bader charge transfer.³²⁻³⁴ Figure 5 shows the ELF cross-sections in the (110)

plane containing both Fe and O atoms for ε -Fe, Fe₃O, Fe₂O, and B8-FeO. In ε -Fe, the ELF is relatively uniform. In B8-FeO, valence electrons are more concentrated near oxygens, while Fe layers maintain a relatively uniform electron density. In Fe₃O and Fe₂O, adjacent Fe-Fe layers show similar ELFs as in ε -Fe, while adjacent Fe-O layers have ELFs like those in B8-FeO. Table 1 shows Bader charge transfers in these compounds. Approximately 0.97 electrons transfer from Fe to O in B8-FeO. In Fe₃O and Fe₂O, O ions gain roughly the same number of electrons, but the electron loss per Fe in Fe₂O is 0.47, i.e., half of that in FeO. In Fe₃O, Fe without O neighbors (Fe₃/Fe₆) shows almost no electron loss, while Fe with O neighbors (Fe₁/Fe₂/Fe₄/Fe₅) shows an electron loss of 0.45, similar to Fe in Fe₂O. Therefore, electronic DOS, chemical bonding, and charge transfer in Fe_nO phases can be interpreted by recalling those in the endmember phases, i.e., ε -Fe and B8-FeO. This seemingly simple and sort-of-short-range interaction between Fe and B8-FeO suggests several stoichiometries are possible in the Fe-FeO system, i.e., Fe_nO phases containing O-only and Fe-only close-packed layers stacked in different ways that depend on *n*. An entropically stabilized alloy with stacking disorder is likely to form at high temperatures.

Geophysical implications. Our high P-T experiments show that Fe and FeO/Fe₂O₃ react at 220– 260 GPa at temperatures higher than 3,000 K. At the same time, our ab initio crystal structure prediction identifies several stable Fe_nO phases with n > 1 at similar pressure conditions. These newly identified phases differ from previously suggested Fe_nO models, ^{13,14} and consist of single species (Fe-only or O-only) close-packed layers in various stacking sequences with O-only single layer always separated by Fe-only layers. The best solutions for the experimental XRD peaks of the new phases quenched to room temperature point to structures lacking long-range chemical or stacking order. Still, with average compositions close to Fe₂O, i.e., that of the most stable phase identified computationally in the Fe-FeO system. With this in mind, the new high-temperature reaction products are likely entropically stabilized solid solutions whose intrinsic disorder is retained upon quenching. Notably, these high entropy phases may be favored over stoichiometric compounds (e.g., Fe₂O and Fe₃O) at high inner core temperatures. In general, the presence of oxygen layers should make Fe_nO alloys more anisotropic from the elastic and thermal transport points of view compared to pure iron. These properties must be carefully investigated since they are essential for understanding the core's thermal evolution and seismic features, including the inner core's age, energy source powering the geodynamo, and seismic heterogeneities.^{35,36}

In addition, this layered alloy structure could also exist in other Fe-light elements, such as hydrogen and carbon.37 (THIS IS SPECULATIVE AND I DON'T THINK IT BELONGS HERE)

Oxygen has been proposed to be a likely light element alloyed with Fe in the liquid OC.⁸ It has been suggested that an oxygen-rich liquid OC adjoining an oxygen-deprived solid IC might account for global seismic observations of the density jump across the IC-OC boundary.¹¹ The successful syntheses of solid Fe-rich Fe_nO phases here suggest that the solid IC may also incorporate a significant amount of oxygen. The result is a less drastic oxygen partitioning between the OC and the IC and, consequently, a more complex origin of this density deficit contrast, with other elements also playing a significant role.⁸ In addition, forming solid Fe-rich Fe_nO phases via IC nucleation and growth would affect the associated latent heat release from the IC to power the geodynamo through geological time.⁴⁶

Oxygen has been present in every stage of Earth's formation and evolution, and chemical interactions in the deep Earth involve oxygen transfer between the core and mantle. ³⁸⁻⁴⁰ It has been suggested that the precipitation of MgO, FeO, and SiO₂ in the OC could have provided gravitational energy to drive early core convection and the Earth's ancient magnetic field before the formation of the Earth's solid inner core. ⁴¹⁻⁴⁵ Incorporation of oxygen in solid Fe_nO phase(s) extends the deep oxygen cycle to the IC and impacts this precipitation process. Future studies of multiple element partitioning, including oxygen, between solid and liquid Fe will help clarify the relative abundances of the light elements, the origin of the density deficit in both regions, and many other processes involving the Earth's core evolution.

Methods

Sample preparation and characterization. Starting materials of pure iron (C.A.S. # 7439-89-6) mixed with FeO (C.A.S. # 1345-25-1) or Fe₂O₃ (C.A.S. # 1309-37-1) powders with grain sizes ranging from submicron to a few microns were prepared in the Fe/O ratio \sim 3:1. Each of the two mixtures was mechanically ground for 90 minutes in a glove box filled with Ar. Pairs of single or double-beveled diamond anvils with culet sizes of 50–300 or 60–180–300 μ m were used for laser-heated diamond anvil cell (DAC) experiments. The sample disk of each Fe-O mixture was compressed to \sim 3 μ m thick and 14–16 μ m across was selected and loaded into a sample chamber measuring 20–25 μ m across consisting of a pre-indented Re gasket. Each sample platelet was

sandwiched between two dried KCl platelets used as the pressure-transmitting medium and thermal insulation layers. The whole DAC sample assembly was sealed in a vacuum using a high-pressure gas loading system after being evacuated for 30 minutes before each sample chamber was compressed to high pressures. Before reaching a target pressure, XRD patterns were collected at ~30 GPa to confirm the presence of both iron and iron oxide.

Synchrotron x-ray diffraction experiments. XRD measurements were conducted at beamlines 13-IDD of the Advanced Phonon Source (A.P.S.), Argonne National Laboratory (A.N.L.). A highly monochromatized x-ray source with an energy of 42 keV (0.2952 Å) was used as the incident x-ray beam and focused down to a 2–5 μm spot size (full width at half maximum (FWHM)) at the sample position. Each DAC was compressed to high pressure at room temperature to prepare for laser heating experiments. The pressure was determined from lattice parameters of hcp-Fe and B2-KCl, generally with an uncertainty of 2–5 GPa.⁴⁷ At targeted pressures, two infrared laser beams were focused on 20–30 μm spots (FWHM) on both sides of the sample. They were coaxially aligned with the incident x-ray beam using the x-ray-induced luminescence on the sample and/or ruby. We estimate the temperature of the heated samples by fitting measured thermal radiation spectra with the gray-body assumption function. The temperature uncertainty was within 100–200 K based on multiple temperature measurements on both sides.

Adaptive genetic algorithm search. We searched for crystal structures of Fe-rich Fe_nO using the adaptive genetic algorithm (AGA),^{28,48,49} which combines *ab initio* calculations and auxiliary interatomic potentials described by the embedded-atom method in an adaptive manner to ensure high efficiency and accuracy. The structure searches were only constrained by the chemical composition, without any assumption on the Bravais lattice type, symmetry, atom basis, or unit cell dimensions. A wide range of different Fe-rich compositions (i.e., 2:1, 3:1, 3:2, 4:1, 4:3, 5:1, 5:2, 5:3, 5:4, 6:1, 6:5, 7:1, 8:1, 9:1) were selected with up to 25 atoms in the unit cell to perform the search. Each AGA run contains a genetic algorithm (GA) loop accelerated by interatomic potential and a density functional theory (DFT) calculation loop to refine the potential. The candidate pool in the GA search contained 64 structures. In each GA generation, 16 new structures were generated from the parent structure pool via the mating procedure. The structures in the pool were updated by keeping the lowest-energy 64 structures. The structure search with a given auxiliary interatomic potential sustained 1,000 consecutive GA generations. After one GA loop, 16 structures were randomly

selected for static DFT calculation to refine the potential. This process was repeated 80 times, followed by DFT structure optimization on unique crystal structures.

Ab initio calculations. We carried out *ab initio* calculations using the projector augmented wave (PAW) method within DFT as implemented in the VASP code. So-52 The exchange and correlation energy are treated with the generalized gradient approximation parameterized by the Perdew-Burke-Ernzerhof formula. PAW potentials with valence electronic configurations $3d^74s^1$ and $2s^22p^4$ were used for Fe and O atoms, respectively. The hard-core PAW potential with $3p^63d^74s^1$ for Fe is also tested. Both Fe PAWs show consistent results (see Supplementary Note 4 and Fig. S17). The Mermin functional is employed. Applied PAGA search, the Monkhorst-Pack sampling scheme was adopted for Brillouin zone sampling with a k-point grid of $2\pi \times 0.033$ Å⁻¹, and the ionic relaxations stopped when the forces on every atom became smaller than 0.01 eV/Å. The energy convergence criterion is 10^{-4} eV. Phonon calculations were performed using density functional perturbation theory implemented in the VASP code and the Phonopy software, with a k-point grid of $2\pi \times 0.033$ Å⁻¹ and supercells of $3 \times 3 \times 2$ for Fe₂O (54 atoms), $2 \times 2 \times 2$ for Fe₃O (64 atoms), $2 \times 2 \times 2$ for Fe₃O₂ rhombohedral lattice (40 atoms) and $2 \times 2 \times 2$ for Fe₄O₃ rhombohedral lattice (56 atoms).

Reverse Monte Carlo (RMC) simulations. The RMC simulations were performed by randomly changing the chemistry (Fe/O ratio) and layer stackings in the supercells of the hexagonal lattice. There is no restriction of overall Fe/O concentration in the supercell. The only criterion to select preferred structures during the random sampling is based on the XRD deviation $D_{XRD} = \sqrt{\langle (I_{exp}(2\theta) - I_{sim}(2\theta))^2 \rangle}$, which is the mean square deviation of intensities between simulated, I_{sim} , and the experimental, I_{exp} , XRDs. The smaller D_{XRD} , the better the agreement with the experimental data. The acceptance rate during the RMC simulation follows the typical Metropolis acceptance rule as $p = e^{-\beta \Delta D}$, where ΔD is the change of XRD deviation between two MC steps. β is a scaling factor that makes the overall acceptance rate around 20%. The structure is updated if the stacking changes during the R.M.C. simulation. The interlayer distances were set using the most probable spacings shown in Fig. 3a. According to Fig. 2d, only seven out of twelve stacking sequences appeared in the low-energy structures found with the A.G.A. search. Stackings other than the seven preferred ones in the R.M.C. simulations were discouraged by assigning large ΔD s.

The R.M.C. simulations used supercells containing 20 to 60 layers. Each simulation was repeated 314 315 independently 30 times.

316 317

318

319

320

321

322

323

324

325

326

327

328

329

330

331

332

333

334

335

340

Reference

- 1. Hirose, K., Labrosse, S. & Hernlund, J. (2013). Composition and state of the core. Annu. Rev. Earth Planet. Sci. 41, 657-691.
 - 2. Birch, F. (1952). Elasticity and constitution of the Earth's interior. J. Geophys. Res. 57, 227-286.
- 3. Poirier, J.-P. (1994). Light elements in the Earth's outer core: A critical review. Phys. Earth Planet. Inter. 85, 319-337.
 - 4. Hirose, K., Wood, B. & Vočadlo, L. (2021). Light elements in the Earth's core. Nat. Rev. Earth Environ. 2, 645-658.
 - 5. Morard, G., Andrault, D., Antonangeli, D. & Bouchet, J. (2014). Properties of iron alloys under the Earth's core conditions. C. R. Geosci. 346, 130-139.
 - 6. Lin, J.-F., Heinz, D. L., Campbell, A. J., Devine, J. M. & Shen, G. (2002). Iron-silicon alloy in Earth's core? Science 295, 313-315.
 - 7. Oka, K. et al. (2019). Melting in the Fe-FeO system to 204 GPa: Implications for oxygen in Earth's core Am. Mineral. 104, 1603-1607.
 - 8. Badro, J., Brodholt, J. P., Piet, H., Siebert, J. & Ryerson, F. J. (2015). Core formation and core composition from coupled geochemical and geophysical constraints. Proc. Natl. Acad. Sci. U.S.A. 112, 12310-12314.
 - 9. Hu, Q. et al. (2016). FeO₂ and FeOOH under deep lower-mantle conditions and Earth's oxygenhydrogen cycles. Nature 534, 241-244.
- 336 10. Liu, J. et al. (2019). Altered chemistry of oxygen and iron under deep Earth conditions. Nat. 337 Commun. 10, 153.
- 338 11. Alfè, D., Gillan, M. J. & Price, G. D. (2000). Constraints on the composition of the Earth's core from 339 ab initio calculations. Nature 405, 172-175.
- 12. Ozawa, H., Hirose, K., Tateno, S., Sata, N. & Ohishi, Y. (2010). Phase transition boundary between 341 B1 and B8 structures of FeO up to 210 GPa. Phys. Earth Planet. Inter. 179, 157-163.
- 342 13. Sherman, D. M. (1995). Stability of possible Fe-FeS and Fe-FeO alloy phases at high pressure and the 343 composition of the Earth's core. Earth Planet. Sci. Lett. 132, 87–98.
- 344 14. Alfè, D., Price, G. D. & Gillan, M. J. (1999). Oxygen in the Earth's core: A first-principles study. 345 Phys. Earth Planet. Inter. 110, 191-210.
- 346 15. Weerasinghe, G. L., Pickard, C. J. & Needs, R. J. (2015). Computational searches for iron oxides at 347 high pressures. J. Phys.: Condens. Matter 27, 455501.

- 16. Fei, Y. & Mao, H. (1994). *In situ* determination of the NiAs phase of FeO at high pressure and temperature. Science *266*, 1678-1680.
- 17. Ozawa, H. *et al.* (2011). Spin crossover, structural change, and metallization in NiAs-type FeO at high pressure. Phys. Rev. B *84*, 134417.
- 18. Weck, G., Desgreniers, S., Loubeyre, P. & Mezouar, M. (2009). Single-crystal structural characterization of the metallic phase of oxygen. Phys. Rev. Lett. *102*, 255503.

357

358

359

360

361

364

365

366

367

368

369

370

371

- 19. Ringwood, A. E. & Hibberson, W. (1990). The system Fe-FeO revisited. Phys. Chem. Miner. *17*, 313-355
 - 20. Ozawa, H., Takahashi, F., Hirose, K., Ohishi, Y. & Hirao, N. (2011). Phase transition of FeO and stratification in Earth's outer core. Science *334*, 792-794.
 - 21. Lavina, B. *et al.* (2011). Discovery of the recoverable high-pressure iron oxide Fe₄O₅. Proc. Natl. Acad. Sci. U.S.A. *108*, 17281-17285.
 - 22. Lavina, B. & Meng, Y. (2015). Unraveling the complexity of iron oxides at high pressure and temperature: Synthesis of Fe₅O₆. Sci. Adv. *1*, e1400260.
- 362 23. Bykova, E. *et al.* (2016). Structural complexity of simple Fe₂O₃ at high pressures and temperatures.
 363 Nat. Commun. 7, 10661.
 - 24. Liu, J. *et al.* (2021). Evidence for oxygenation of Fe-Mg oxides at mid-mantle conditions and the rise of deep oxygen. Natl. Sci. Rev. *8*, nwaa096.
 - 25. Chen, B. *et al.* (2014). Hidden carbon in Earth's inner core revealed by shear softening in dense Fe₇C₃. Proc. Natl. Acad. Sci. U.S.A. *111* 17755-17758.
 - 26. Prescher, C. *et al.* (2015). High Poisson's ratio of Earth's inner core explained by carbon alloying. Nat. Geosci. *8*, 220-223.
 - 27. Liu, J., Lin, J. F., Prakapenka, V. B., Prescher, C. & Yoshino, T. (2016). Phase relations of Fe₃C and Fe₇C₃ up to 185 GPa and 5200 K: Implication for the stability of iron carbide in the Earth's core. Geophys. Res. Lett. *43*, 12415-12422.
- Wu, S. Q. *et al.* (2014). An adaptive genetic algorithm for crystal structure prediction. J. Phys.:
 Condens. Matter 26, 035402.
- 29. Zhang, Z., Zhang, D. B., Sun, T. & Wentzcovitch, R. M. (2019). phq: A Fortran code to compute
 phonon quasiparticle properties and dispersions. Comput. Phys. Commun. 243, 110-120.
- 30. Sun, Y. *et al.* (2022). Ab initio melting temperatures of bcc and hcp iron under the Earth's inner core condition. arXiv:2205.02290.
- 31. Zhang, D.-B., Sun, T. & Wentzcovitch, R. M. (2014). Phonon quasiparticles and anharmonic free energy in complex systems. Phys. Rev. Lett. *112*, 058501.

- 32. Becke, A. D. & Edgecombe, K. E. (1990). A simple measure of electron localization in atomic and molecular systems. J. Chem. Phys. *92*, 5397.
- 33. Silvi, B. & Savin, A. (1994). Classification of chemical bonds based on topological analysis of electron localization functions. Nature *371*, 683-686.
- 34. Henkelman, G., Arnaldsson, A. & Jónsson, H. (2006). A fast and robust algorithm for Bader decomposition of charge density. Comput. Mater. Sci. *36*, 354-360.

388

389

390

391

392

393

394

395

396

397

398

399

400

401

402

403

404

405

406

- 35. Hsieh, W.-P. *et al.* (2020). Low thermal conductivity of iron-silicon alloys at Earth's core conditions with implications for the geodynamo. Nat. Commun. *11*, 3332.
- 36. Zhang, Y. *et al.* (2020). Reconciliation of experiments and theory on transport properties of iron and the geodynamo. Phys. Rev. Lett. *125*, 078501.
- 37. Li, Y., Vočadlo, L., Alfè, D. & Brodholt, J. (2019). Carbon partitioning between the Earth's inner and outer core. J. Geophys. Res. *124*, 12812-12824.
 - 38. Knittle, E. & Jeanloz, R. (1991). Earth's core-mantle boundary: Results of experiments at high pressures and temperatures. Science *251*, 1438-1443.
- 39. Takafuji, N., Hirose, K., Mitome, M. & Bando, Y. (2005). Solubilities of O and Si in liquid iron in equilibrium with (Mg,Fe)SiO₃ perovskite and the light elements in the core. Geophys. Res. Lett. *32*, L06313.
 - 40. Tsuno, K., Frost, D. J. & Rubie, D. C. (2013). Simultaneous partitioning of silicon and oxygen into the Earth's core during early Earth differentiation. Geophys. Res. Lett. *40*, 66-71.
 - 41. O'Rourke, J. G. & Stevenson, D. J. (2016). Powering Earth's dynamo with magnesium precipitation from the core. Nature *529*, 387-389.
 - 42. Badro, J., Siebert, J. & Nimmo, F. (2016). An early geodynamo driven by exsolution of mantle components from Earth's core. Nature *536*, 326-328.
 - 43. Hirose, K. *et al.* (2017). Crystallization of silicon dioxide and compositional evolution of the Earth's core. Nature *543*, 99-102.
 - 44. Davies, C. J., Pozzo, M., Gubbins, D. & Alfè, D. (2020). Transfer of oxygen to Earth's core from a long-lived magma ocean. Earth Planet. Sci. Lett. *538*, 116208.
- 45. Zhang, Z. *et al.* (2022). Free energies of Fe-O-Si ternary liquids at high temperatures and pressures:
 Implications for the evolution of the Earth's core composition. Geophys. Res. Lett., e2021GL096749.
- 46. O'Rourke, J. G., Korenaga, J. & Stevenson, D. J. (2017). Thermal evoution of Earth with magnesium
 precipitation in the core. Earth and Planatary Science Letters, 263-272.
- 47. Dewaele, A. *et al.* (2012). High-pressure–high-temperature equation of state of KCl and KBr. Phys.
 413 Rev. B *85*, 214105.

- 48. Deaven, D. M. & Ho, K. M. (1995). Molecular geometry optimization with a genetic algorithm. Phys. Rev. Lett. *75*, 288–291.
- 49. Zhao, X. *et al.* (2014). Exploring the structural complexity of intermetallic compounds by an adaptive genetic algorithm. Phys. Rev. Lett. *112*, 045502.
- 418 50. Blöchl, P. E. (1994). Projector augmented-wave method. Phys. Rev. B 50, 17953-17979.
- 51. Kresse, G. & Furthmüller, J. (1996). Efficiency of ab-initio total energy calculations for metals and semiconductors using a plane-wave basis set. Comput. Mater. Sci. 6, 15-50.
- 52. Kresse, G. & Furthmüller, J. (1996). Efficient iterative schemes for ab initio total-energy calculations using a plane-wave basis set. Phys. Rev. B *54*, 11169-11186.
- 53. Perdew, J. P., Burke, K. & Ernzerhof, M. (1996). Generalized gradient approximation made simple.
 Phys. Rev. Lett. 77, 3865-3868.

427

428

429

430

431

432

433

434

435

436

437

438

439

440

445

- 54. Mermin, N. D. (1965). Thermal properties of the inhomogeneous electron gas. Phys. Rev. *137*, A1441.
- 55. Wentzcovitch, R. M., Martins, J. L. & Allen, P. B. (1992). Energy versus free-energy conservation in first-principles molecular dynamics. Phys. Rev. B *45*, 11372.
- 56. Monkhorst, H. J. & Pack, J. D. (1976). Special points for Brillouin-zone integrations. Phys. Rev. B 13, 5188-5192.
- 57. Baroni, S., de Gironcoli, S., Dal Corso, A. & Giannozzi, P. (2001). Phonons and related crystal properties from density-functional perturbation theory. Rev. Mod. Phys. *73*, 515-562.
- 58. Togo, A. & Tanaka, I. (2015). First principles phonon calculations in materials science. Scr. Mater. *108*, 1-5.
 - 59. Wentzcovitch, R. M., Yu, Y. G. & Wu, Z. (2010). Thermodynamic properties and phase relations in mantle minerals investigated by first principles quasiharmonic theory. Rev. Mineral. Geochem. 71, 59-98.
- 60. Qin, T., Zhang, Q., Wentzcovitch, R. M. & Umemoto, K. (2019). qha: A Python package for quasiharmonic free energy calculation for multi-configuration systems. Comput. Phys. Commun. 237, 199-207.
- 441 61. Palasyuk, O. *et al.* (2021). Structural and magnetic properties of hard magnetic system Ce(Co₁-442 $_x$ Fe_x)_{4.4}Cu_{0.6} ($0 \le x \le 0.19$). J. Alloys Compd. **883**, 160866.
- 62. Alfè, D., Gillan, M. J. & Price, G. D. (2007). Temperature and composition of the Earth's core.
 Contemp. Phys. 48, 63-80.

Acknowledgements

This work is supported by the NSFC Grants no. 42072052 and U1930401, by the National Science Foundation awards EAR-1918126 (R.M.W. and Y.S.), EAR-1918134 (K.-M.H. and C.Z.W), and EAR-1901808 and EAR-1916941 (J.-F.L.). R.M.W. also acknowledges partial support from the Department of Energy, Theoretical Chemistry Program through grant DE-SC0019759. Computational resources were provided by the Extreme Science and Engineering Discovery Environment (XSEDE) funded by the National Science Foundation through award ACI-1548562. This research also used resources of the Advanced Photon Source (A.P.S.), a U.S. Department of Energy (D.O.E.) Office of Science User Facility operated by Argonne National Laboratory under Contract No. DE-AC02-06CH11357. The GeoSoilEnviroCARS at A.P.S. is supported by the National Science Foundation - Earth Sciences award EAR-1634415 and the Department of Energy-GeoSciences award DE-FG02-94ER14466. Some experiments are supported by the Synergic Extreme Condition User Facility (SECUF) and beamline BL15U1 at the Shanghai Synchrotron Radiation Facility (SSRF).

Author contributions

J.-F.L., J.L., R.M.W., and Y.S. conceived the project. Y.S., F.Z., C.Z.W, and K.M.H. performed *ab initio* calculations and crystal structure search. J.L., J.-F.L., C.L., S.F., and V.B.P. carried out synchrotron experiments and data analyses. J.L., Y.S., and R.M.W. wrote the manuscript. All authors discussed the results and contributed to paper writing.

Competing interests

The authors declare no competing interests.

Data availability

All original data supporting the findings and structure files of this study have been deposited: https://doi.org/10.5281/zenodo.5650734. Additional data are available upon request from the corresponding authors. Source data are provided in this paper.

Code availability

The Vienna Ab initio Simulation Package is proprietary software available for purchase at http://www.vasp.at/. The Phonopy code is available at http://www.vasp.at/. The Phonopy code is available at https://phonopy.github.io/phonopy/.

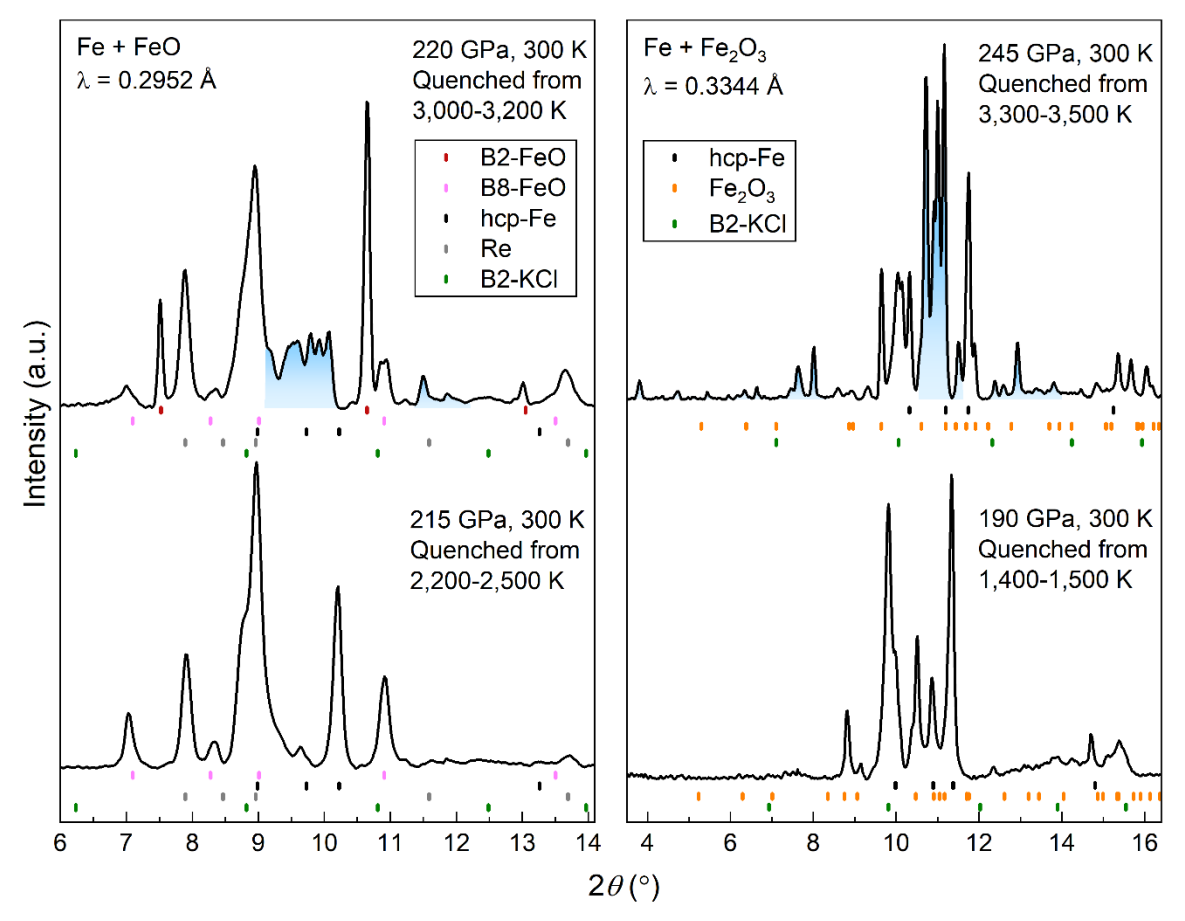


Figure 1 | Typical X-ray diffraction patterns of quenched samples collected before and after the reaction of Fe with FeO at 220 GPa and Fe₂O₃ at 245 GPa at high temperatures. Left panel: B8-FeO has lattice parameters a=2.3480(17) Å and c=4.7901(41) Å; hcp-Fe has a=2.1792(19) Å and c=3.4865(32) Å; hcp-Re has a=2.4733 (23) Å and c=3.9944(47) Å; cubic B2-KCl has a=2.7292(53) Å at 215-220 GPa and room temperature; B2 denotes B2-FeO. Right panel: Starting materials were a mixture of iron and hematite; hcp-Fe has a=2.2195(81) Å and c=3.5220(115) Å at 190 GPa, and a=2.1489(68) Å and c=3.4391(95) Å at 245 GPa and room temperature; Fe₂O₃ has a=2.2903(57) Å, b=7.3913(116) Å and c=5.5172(81) Å at 190 GPa, and a=2.2412(45) Å, b=7.2328(103) Å and c=5.3989(81) Å at 245 GPa and room temperature; cubic B2-KCl has a=2.7705(64) Å at 190 GPa and a=2.7024(71) Å at 245 GPa at room temperature. Vertical ticks: ϵ -Fe (black), B2-FeO (red), B8-FeO (magenta), post-perovskite Fe₂O₃ (orange), B2-KCl (olivine), and Re gasket (grey). Blue shaded areas highlight some of the new diffraction peaks that emerged at the expense of Fe and FeO/Fe₂O₃ peaks when the temperature reaching 3,000-3,200 at 220 GPa and 3,300-3,500 K at 245 GPa, respectively (see Figs. S3-S4 for the indexing to the reaction products).

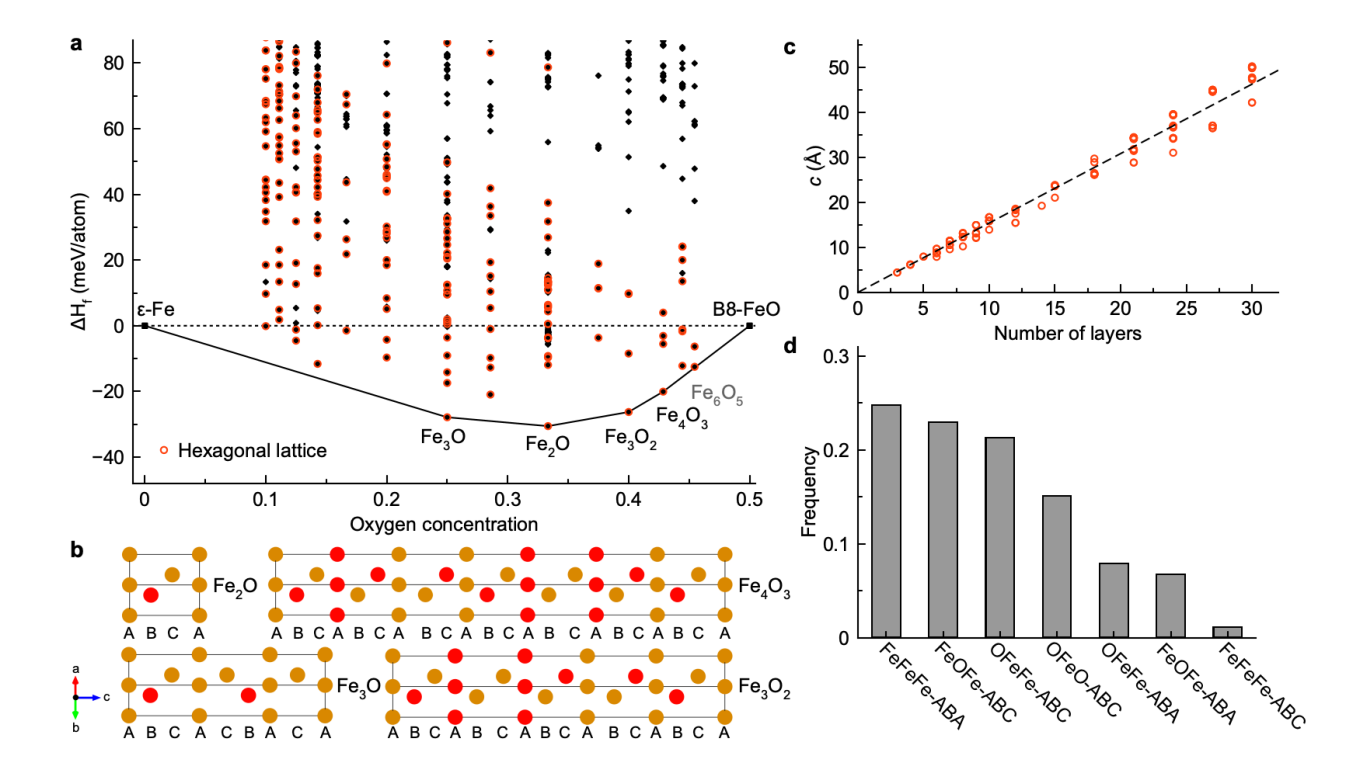


Figure 2 | Crystal structure of identified Fe_nO compounds at 215 GPa. (a) The formation enthalpy of AGA-searched compounds referenced by the dashed line shows their relative stability relative to the decomposition into ε -Fe and B8-FeO. The solid line indicates the convex hull formed by the thermodynamically stable compounds. Red symbols show structures with hexagonal close-packed layers. (b) Crystal structures of four Fe-rich compounds in the ground states. Gold and red circles represent iron and oxygen, respectively. (c) Lattice parameter c of low-energy close-packed crystals as a function of the number of layers. (d) Frequency of structural and chemical order in the nearest neighbor layers of the low-energy close-packed crystals.

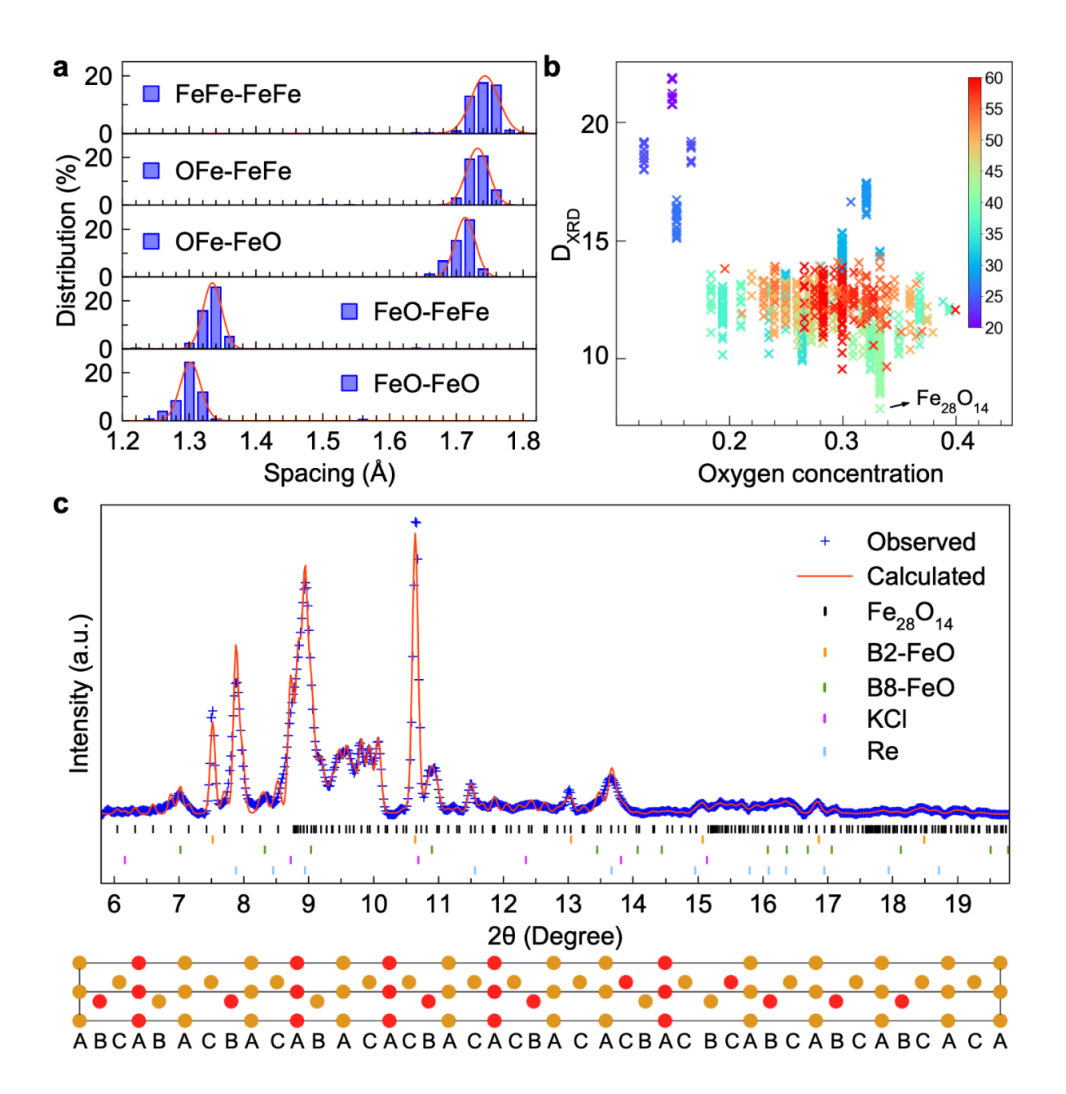


Figure 3 | Reverse Monte Carlo simulation of Fe₂₈O₁₄ structure. (a) Distribution of middle layer spacings with different neighboring layers. Legends indicate chemical elements in the first and second nearest neighbor layers, e.g., "OFe-FeO" denoting that Fe layers are the first nearest neighbor and O layers are the second nearest neighbors. The red curve is a Gaussian distribution fitting. (b) Oxygen concentration and XRD deviation (D_{XRD}) of supercell structures from RMC simulation. Each point represents the final structure from one R.M.C. simulation. The color bar indicates the number of atoms in the supercell. (c) The comparison between diffraction patterns by experiments at 220 GPa and the Fe₂₈O₁₄ supercell XRD produced by RMC simulations. The incident x-ray wavelength (λ) is 0.2952 Å. Vertical ticks: Fe₂₈O₁₄ (black), B2-FeO (orange), B8-FeO (green), B2-KCl (magenta), and hcp-Re (blue). The lower panel shows the simulated crystal structure of Fe₂₈O₁₄.

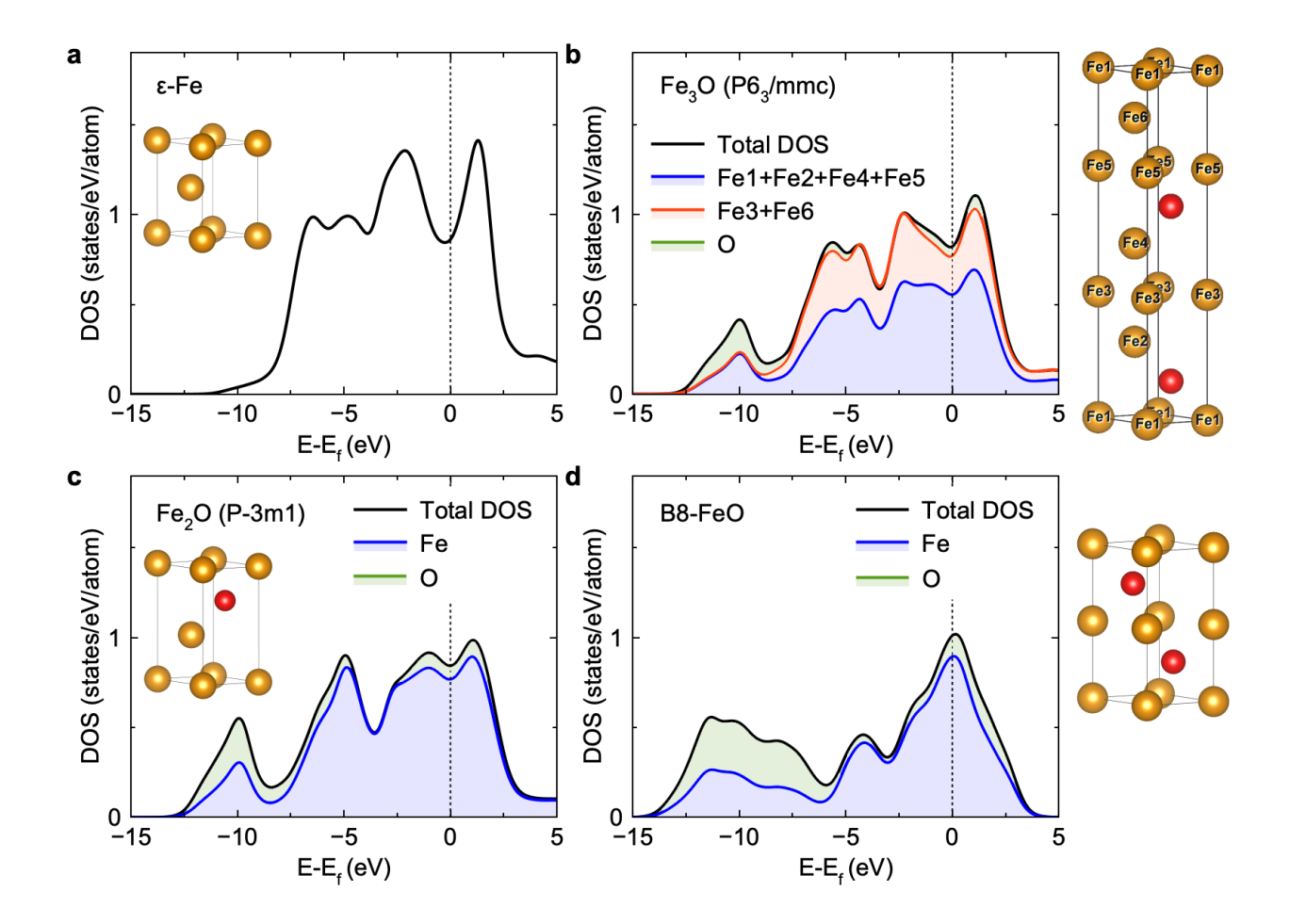


Figure 4 | Projected DOS of Fe 3d electrons in Fe and Fe_nO compounds at 220 GPa and T_{el} = 3,000 K. (a) ϵ -Fe. The dashed line indicates the Fermi level. (b) Fe₃O (space group $P6_3/mmc$). The blue area shows the partial DOS of Fe ions with oxygen neighbor layers (i.e., Fe1, Fe2, Fe4, and Fe5 shown in the crystal structure), while the red area shows the partial DOS of Fe ions without oxygen neighbors (Fe3, Fe6). The green area shows the partial DOS of O. (c) Fe₂O ($P\overline{3}m1$). (d) B8-FeO. Gold and red spheres represent iron and oxygen ions, respectively. The DOS is normalized by dividing the total number of atoms in the cell.

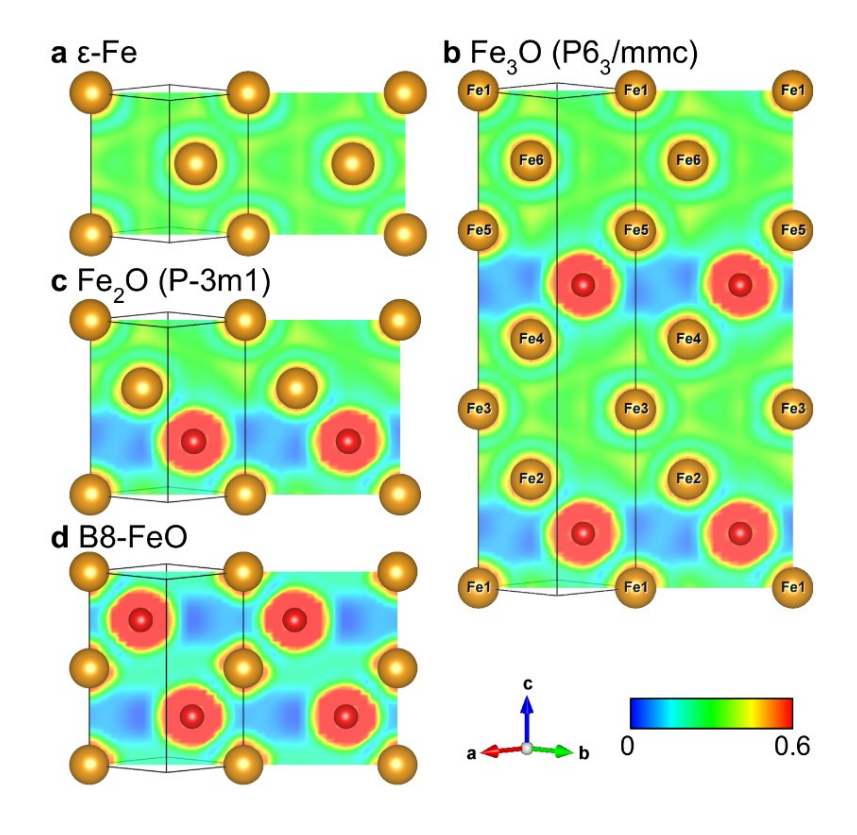


Figure 5 | Electron localization function. (a) ϵ -Fe, (b) Fe₃O (space group $P6_3/mmc$), (c) Fe₂O ($P\overline{3}m1$), and (d) B8-FeO. Gold and red spheres represent iron and oxygen, respectively.

Table 1 | Bader charge analysis of the Fe_nO phases. The indices of Fe in Fe₃O correspond to those in Figs. 4b and 5.

| Phase | Fe | O |
|--|--|-------|
| ε-Fe | 0 | \ |
| Fe ₃ O (<i>P</i> 6 ₃ / <i>mmc</i>) | Fe1/Fe2/Fe4/Fe5: +0.45 Fe3/Fe6: +0.01 | -0.91 |
| $Fe_2O(P\overline{3}m1)$ | +0.47 | -0.94 |
| B8-FeO | +0.97 | -0.97 |

| 539 | Supplementary Materials |
|---|---|
| 540 | |
| 541 | Iron-rich Fe-O compounds at Earth's core pressures |
| 542 543 544 | Jin Liu ^{1,2#*} , Yang Sun ^{3#} , Chaojia Lv ¹ , Feng Zhang ⁴ , Suyu Fu ⁵ , Vitali B. Prakapenka ⁶ , Cai-Zhuang Wang ⁴ , Kai-Ming Ho ⁴ , Jung-Fu Lin ^{5*} , Renata M. Wentzcovitch ^{3,7,8*} |
| 545 546 547 548 549 550 551 552 553 554 555 556 557 | ¹ Center for High Pressure Science and Technology Advanced Research, Beijing 100094, China ² CAS Center for Excellence in Deep Earth Science, Guangzhou, 510640, China ³ Department of Applied Physics and Applied Mathematics, Columbia University, New York, NY 10027, USA ⁴ Department of Physics, Iowa State University, Ames, Iowa 50011, USA ⁵ Department of Geological Sciences, Jackson School of Geosciences, The University of Texas at Austin, Austin, TX 78712, USA ⁶ Center for Advanced Radiation Sources, University of Chicago, Chicago, IL 60439, USA ⁷ Department of Earth and Environmental Sciences, Columbia University, New York, NY 10027, USA ⁸ Lamont–Doherty Earth Observatory, Columbia University, Palisades, NY 10964, USA |
| 558 | |
| 559 | |
| 560 | |
| 561 | |
| 562 | |
| 563 | SUPPLEMENTARY MATERIALS |
| 564 | Supplementary Notes 1-4 |
| 565 | Supplementary Figures S1-S17 |
| 566 | |

Supplementary Note 1 | Experimental XRD patterns and the examination of Fe-C solution.

We employed repetitive laser pulses to reduce the likelihood of breaking diamond anvils significantly. Short heating durations of a few µs in each pulse reduce carbon diffusion and contamination from the sample chamber by the diamond anvils. A few XRD patterns obtained from different experimental conditions and post-analysis are shown in Figs. S1–S7. Fig. S1 shows the XRD without reaction at 183 GPa and 2,000 K. Fig. S2 shows high-pressure and high-temperature XRDs at ~200–260 GPa, 2,200–3,500 K. Figs. S3 and S4 show room-temperature XRDs with the Fe₂₅O₁₃ and Fe₂₈O₁₄ solutions, respectively. Fig. S5 shows the room-temperature XRD of quenched samples in *d*-spacing units. Fig. S6 shows the comparison between room-temperature XRD and known oxygen-rich FeO compounds.

To rule out the possibility of a reaction between Fe and C from the DAC, we compare in Fig. S7 XRD patterns of known Fe-C compounds with the experimental XRD data at room temperature and 220 GPa and 245 GPa. Fe₃C (*Pnma*) and Fe₇C₃ (*Pbca*) are the two main Fe-C compounds stable under high *P-T* conditions relevant to our experiments.²⁵⁻²⁷ At 220 GPa, neither Fe₃C nor Fe₇C₃ can explain the prominent unrecognized diffraction peaks in the 9.6 to 10.2 degrees range. At 245 GPa, Fe₃C or Fe₇C₃ cannot explain the unrecognized diffraction peaks in the 11.0 to 11.3 degrees range either. These factors exclude the two Fe-C phases as the main reason for the additional XRD peaks in the current data.

Supplementary Note 2 | Equation of states of the close-packed Fe_nO phases.

To further validate the supercell model of $Fe_{28}O_{14}$, we compared its static equation of state (EoS) with the experimental data collected upon decompression at room temperature (Fig. S12). The comparison demonstrates the current model well describes the compressive behavior of the reaction product. The slightly smaller calculated volumes of $Fe_{28}O_{14}$ are expected owing to the absence of vibrational effects in the calculation. Fe $Fe_{28}O_{14}$ model is too large and anisotropic to perform phonon calculations with the frozen phonon method or density functional perturbation theory. Therefore, to evaluate the vibrational contribution, we use the $Fe_{2}O$ ground state structure ($P\bar{3}m1$ phase in the main text) and compute the static and the 300K EoSs using the quasiharmonic approximation (QHA). The vibrational effect on the EoS of $Fe_{2}O$ at 300 K is shown in Fig. S12. A similar effect is anticipated in the EoS of $Fe_{28}O_{14}$, which improves agreement between calculated and measured volumes at 300 K. The difference between the static volumes of the $Fe_{28}O_{14}$ structure

model and Fe₂O can be attributed to the disordered nature of Fe₂₈O₁₄. The remaining difference is typical of *ab initio* calculations.

Supplementary Note 3 | Chemical and structural orders in the Fe_nO close-packed hexagonal lattices.

We analyzed the chemical and structural orders of the supercells obtained from Reverse Monte Carlo (RMC) simulations (Fig. 3 in the main text and Fig. S13) to explore the meaning of these solutions. We smeared the iron density profile along the *c* direction using a Gaussian with FWHM of 9.0 Å, corresponding to ~6-layer spacings. Figure S14 shows that the Fe₂₈O₁₄ and Fe₂₅O₁₃ structures have significant compositional variations in the nanometer scale ranging from Fe₅O₂ to Fe₃O₂. Although the average Fe/O ratio of the initial Fe-FeO sample mixture was 3:1, the laser-heated spot centered around a FeO-rich area and the main reaction product appears to have a composition of Fe₂O or nearly so. This is not surprising since Fe₂O is the most stable (with the lowest formation enthalpy) composition in the convex hull. Still, without knowing the phase diagram in detail, it is impossible to predict if the reaction would have followed to completion to produce a phase with an average composition of Fe₃O had the sample been heated longer. The fast reaction process likely causes compositional fluctuations during the short laser heating period. Rapid quenching of an entropically stabilized high-temperature phase also contributes to the observed disorder.

A characteristic feature of the XRD patterns at 220 and 245 GPa is their multi-peaks structure in a small 2θ range. To explore the origin of these peaks, we plot the corresponding lattice planes in the supercell. As shown in Fig. S15a and b, the three main XRD peaks at 220 GPa correspond to the Miller indices (0,1,18), (0,1,-17), and (0,1,16). The main peaks at 245 GPa correspond to indices (0,1,14), (0,1,-13) and (0,1,-11). The corresponding lattice planes are shown in Fig. S15c and d. Visual examination of these structures reveals multi-layer domains with distinct stacking types. They are more easily distinguished by tilting the paper and examining these figures horizontally with the line of sight parallel to the lines specifying the crystalline planes. In both cases, two major domains can be identified in Fig. S16a and b. In Fe₂₈O₁₄, domain A is Fe₁₆O₈, while domain B is Fe₁₂O₆. They contribute differently to the peak intensities. As shown in Fig. S16c, domain A mainly contributes to (0,1,18) and (0,1,-17) peaks, while domain B largely contributes to (0,1,16) and (0,1,14) peaks. Neither of the single domains can fully describe the

XRD. Interference among them is also important as it leads to the suppression of the (0,1,15) peak. Similar behavior is observed in the Fe₂₅O₁₃ supercell in Fig. S16d.

These analyses conclude that these supercell solutions represent structures lacking long-range stacking or chemical order. However, they display medium-range structural order (MRO), i.e., domains with preferred stacking order but lacking chemical order at the scale of ~20 atomic layers or ~30 Å. Similar structures have been observed in layered alloys produced from high-temperature solid solutions⁶¹. The combination and interferences of the MRO domains give rise to complex multi-peak patterns in the current experimental XRD.

Supplementary Note 4 | Consistency of PAW potentials.

We used projector augmented wave (PAW) potentials from the VASP software with the valence electron of $3d^74s^1$ for Fe (noted as PAW8) and $2s^22p^4$ for O. This PAW8 potential is more efficient for the structure optimization in the crystal structure prediction algorithm with thousands of structures. PAW8 was previously used to discover FeO₂ and showed predictive accuracy⁹.

Here, we study the effect of PAW potential by comparing the enthalpy of the Fe_nO compounds using the hard-core Fe potential with valence electron of $3p^63d^74s^1$ (noted as PAW16). Fig. S17a shows that using PAW16, the enthalpy values of the predicted lowest-enthalpy structures are systematically lower than those predicted using PAW8. However, it is the enthalpy of formation that determines relative stabilities. The formation enthalpies calculated by the two PAW potentials differ by less than ~3 meV/atom, as shown in Fig. S17b. Both PAW potentials produce similar convex hulls. Therefore, PAW8 is sufficiently accurate to describe the Fe_nO phases at pressures of interest.

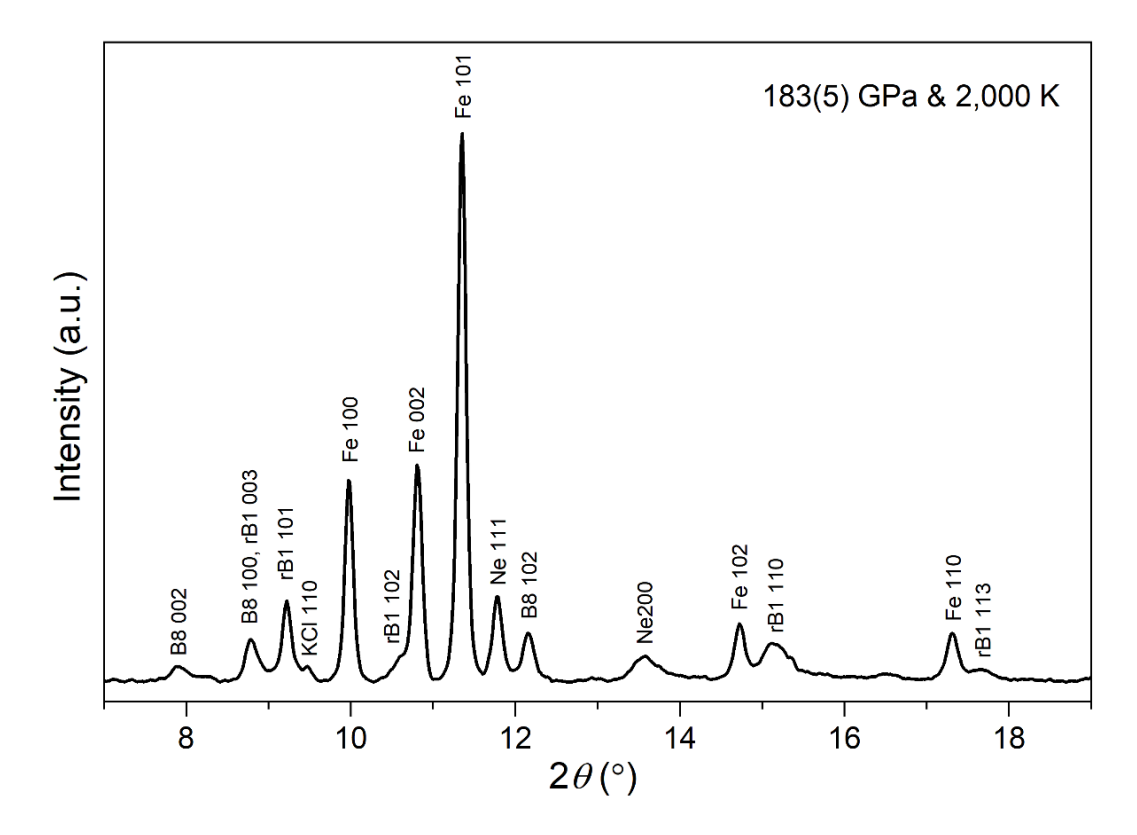


Figure S1 | Representative x-ray diffraction pattern collected at 183 GPa and 2000 K. A mixture of Fe and FeO was used as starting materials. B8 and rB1 labels denote the NiAs-type (B8) and rhombohedral (rB1) phases of FeO, respectively. The x-ray wavelength (λ) used is 0.3344 Å. Known structures explain all peaks.

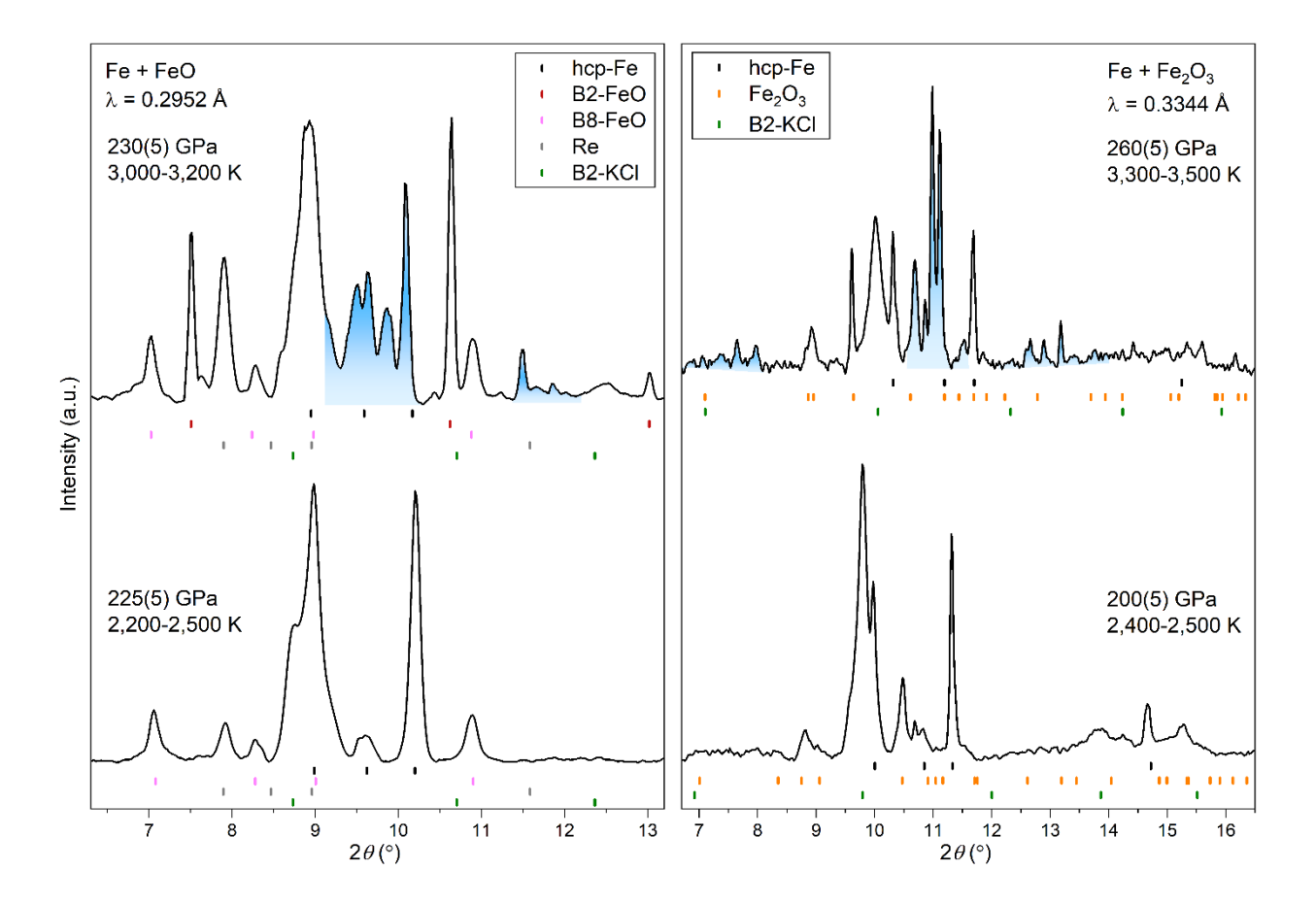


Figure S2 | Representative x-ray diffraction patterns collected at simultaneously high-pressure and high-temperature conditions before and after the reaction of Fe with FeO (left) and Fe₂O₃ (right). Left panel: The mixture of polycrstalline Fe and FeO was used as starting material. B2 and B8 labels denote the CsCl-type (B2) and NiAs-type (B8) phases of FeO, respectively. The x-ray wavelength (λ) used is 0.2952 Å. Right panel: The mixture of polycrystalline Fe and Fe₂O₃ was used as starting material, with KCl used as the pressure-transmitting medium and pressure calibrant. The x-ray wavelength (λ) used is 0.3344 Å. The blue areas highlight some of the new diffraction peaks that emerged at the expense of Fe and FeO peaks when the temperature reached 3,000–3,200 K at pressures greater than 220 GPa. Vertical ticks: ϵ -Fe (black), B2-FeO (red), B8-FeO (magenta), post-perovskite Fe₂O₃ (orange), B2-KCl (olivine), and Re gasket (grey).

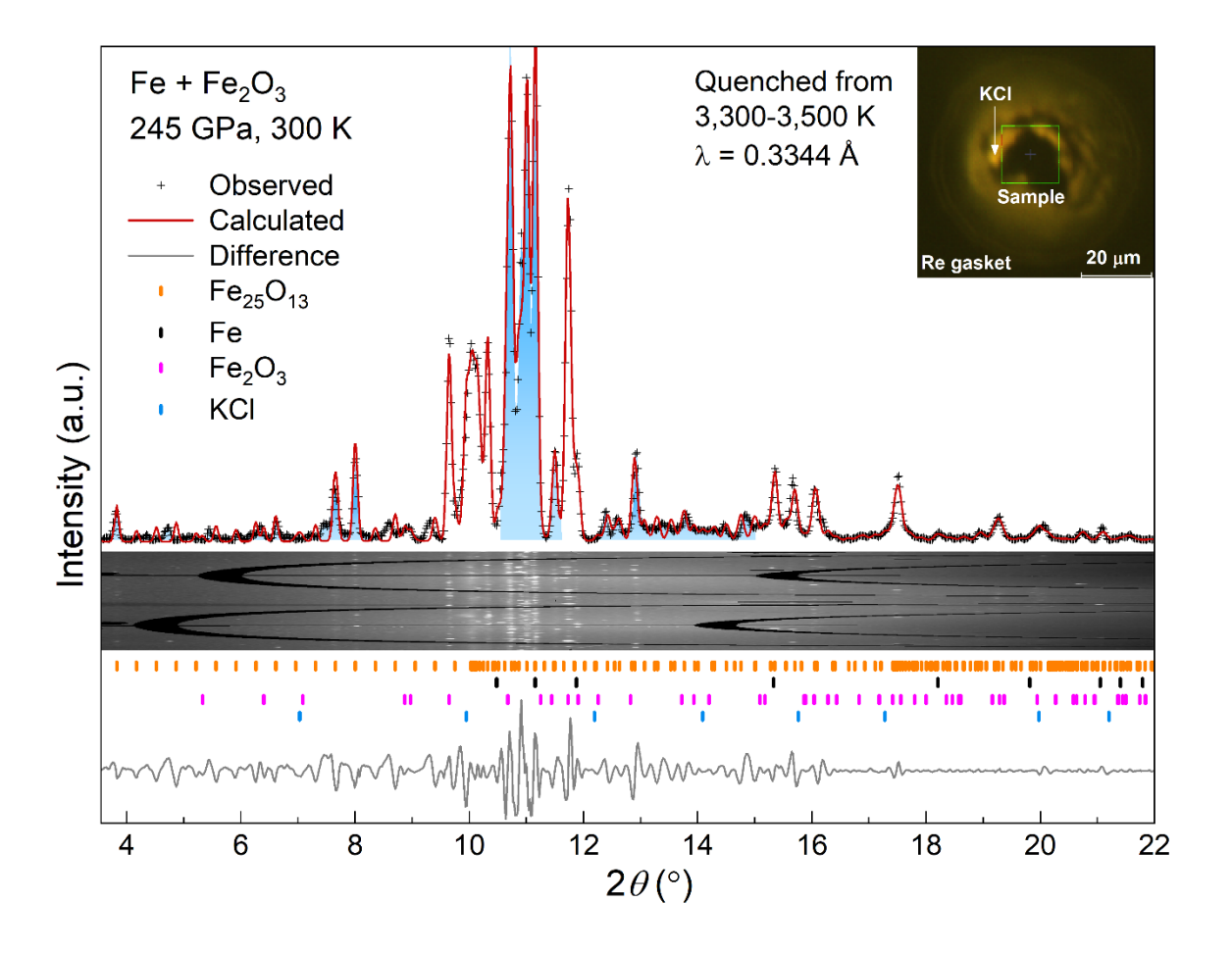


Figure S3 | Representative XRD pattern of iron and hematite Fe₂O₃ reaction products at core pressures at 245 GPa. The pattern at 245 GPa was collected at room temperature after the laser-heated sample was quenched from 3,300–3,500 K at 250–260 GPa. The red curve denotes the Le Bail refinements, whereas the gray line represents the refinement residue. Vertical ticks: hexagonal Fe₂₅O₁₃ (orange), ε-Fe (black), post-perovskite Fe₂O₃ (magenta), and B2-KCl (blue). The mixture of polycrystalline Fe and α-Fe₂O₃ (hematite) was used as starting material. KCl served as pressure calibrant and thermal insulation, as shown in the inset. Re is the gasket material. The x-ray wavelength (λ) was 0.3344 Å. The blue areas highlight some of the new diffraction peaks. The Fe₂₅O₁₃ supercell has a = 2.2082(34) Å and c = 55.082(49) Å; cubic B2-KCl has a = 2.7024(71) Å; Fe₂O₃ (space group: *Cmcm*) has a = 2.2379(45) Å, b = 7.1934(103) Å and c = 5.4094(81) Å; hcp-Fe has a = 2.1489(68) Å and c = 3.4391(95) Å.

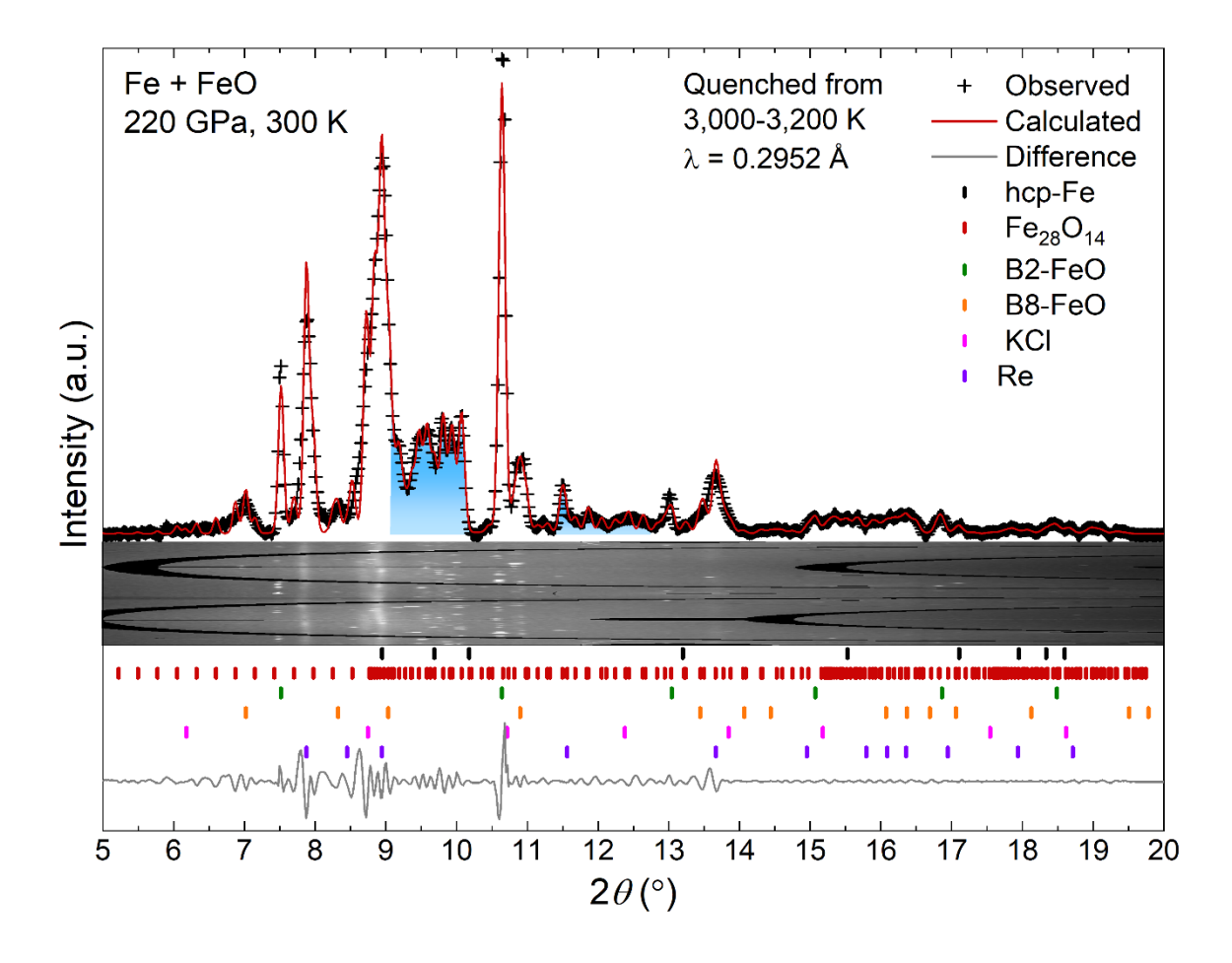


Figure S4 | Representative XRD pattern of iron and wüstite (FeO) reaction products at 220 GPa. The pattern at 220 GPa was collected at room temperature after the laser-heated sample was quenched from 3,000–3,200 K at 230–235 GPa. The new phase(s) emerged at the expense of Fe and FeO when the temperature surpassed 3,000 K. B8-FeO has lattice parameters a = 2.3480(17) Å and c = 4.7901(41) Å; hcp-Fe has a = 2.1792(19) Å and c = 3.4865(32) Å; hcp-Re has a = 2.4733(23) Å and c = 3.9944(47) Å; cubic B2-KCl has a = 2.7292(53) Å; The Fe₂₈O₁₄ supercell has a = 2.2287(45) Å and c = 61.546(78) Å. The blue areas highlight some of the new diffraction peaks.

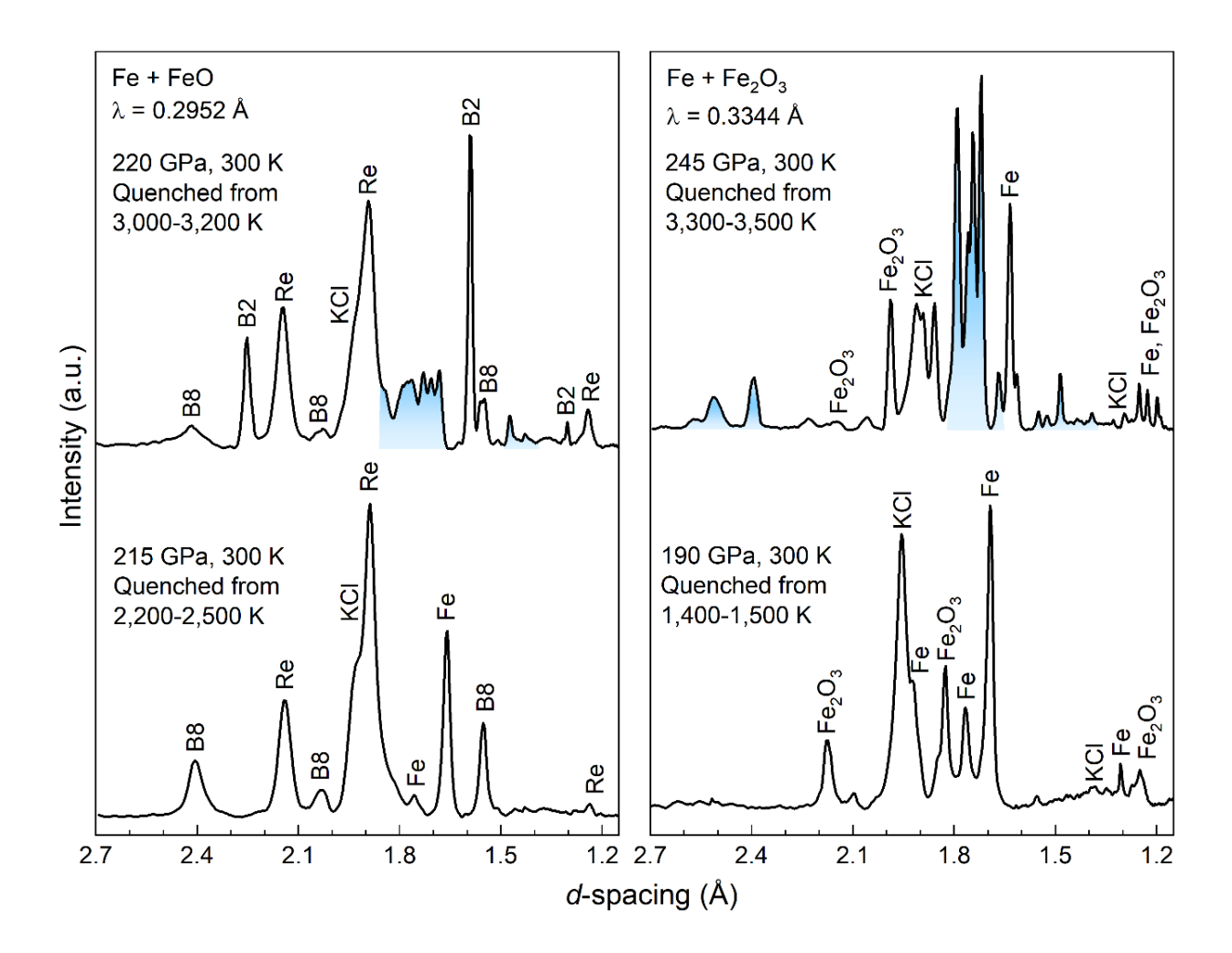


Figure S5 | Room-temperature x-ray diffraction patterns as a function of the *d*-spacing from the reaction of Fe with FeO (left) and Fe₂O₃ (right). The blue areas highlight some of the new diffraction peaks that emerged at the expense of Fe and FeO/Fe₂O₃ peaks when the temperature reached 3,000–3,200 at 220 GPa and 3,300–3,500 K at 245 GPa, respectively. Left panel: B8-FeO has lattice parameters a = 2.3480(17) Å and c = 4.7901(41) Å; hcp-Fe has a = 2.1792(19) Å and c = 3.4865(32) Å; hcp-Re has a = 2.4733 (23) Å and c = 3.9944(47) Å; cubic B2-KCl has a = 2.7292 (53) Å; B2 denotes B2-FeO. Right panel: Starting materials were iron and hematite (Fe₂O₃). The pattern is obtained by transforming 2θ in Fig. 1 to *d*-spacing.

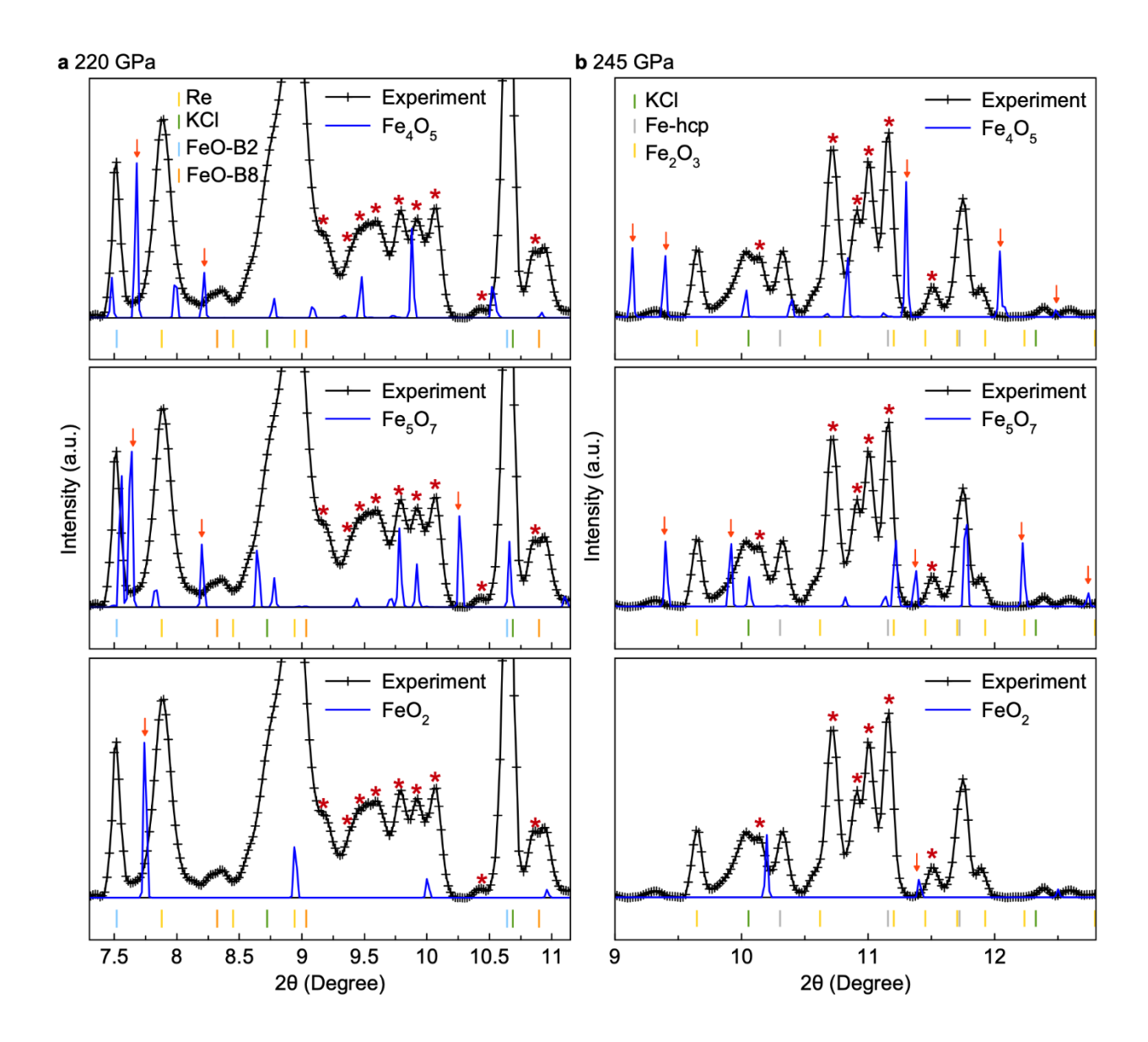


Figure S6 | Comparison between experimental x-ray diffraction patterns and those of oxygen-rich Fe-O compounds. The XRD patterns were collected from (a) Fe+FeO reaction at 220 GPa and (b) Fe+Fe₂O₃ reaction at 245 GPa at room temperature. Blue lines indicate the XRD of oxygen-rich Fe-O compounds. $^{10,21-24}$ Arrows indicate extra peaks of oxygen-rich Fe-O compounds. The x-ray wavelength (λ) was 0.2952 Å for the reaction product of Fe and FeO at 220 GPa, and that was 0.3344 Å for the reaction product of Fe and Fe₂O₃ at 245 GPa. The asterisk symbol (*) represents the diffraction peak of the new phase. No oxygen-rich Fe-O phase could match new experimental diffraction peaks.

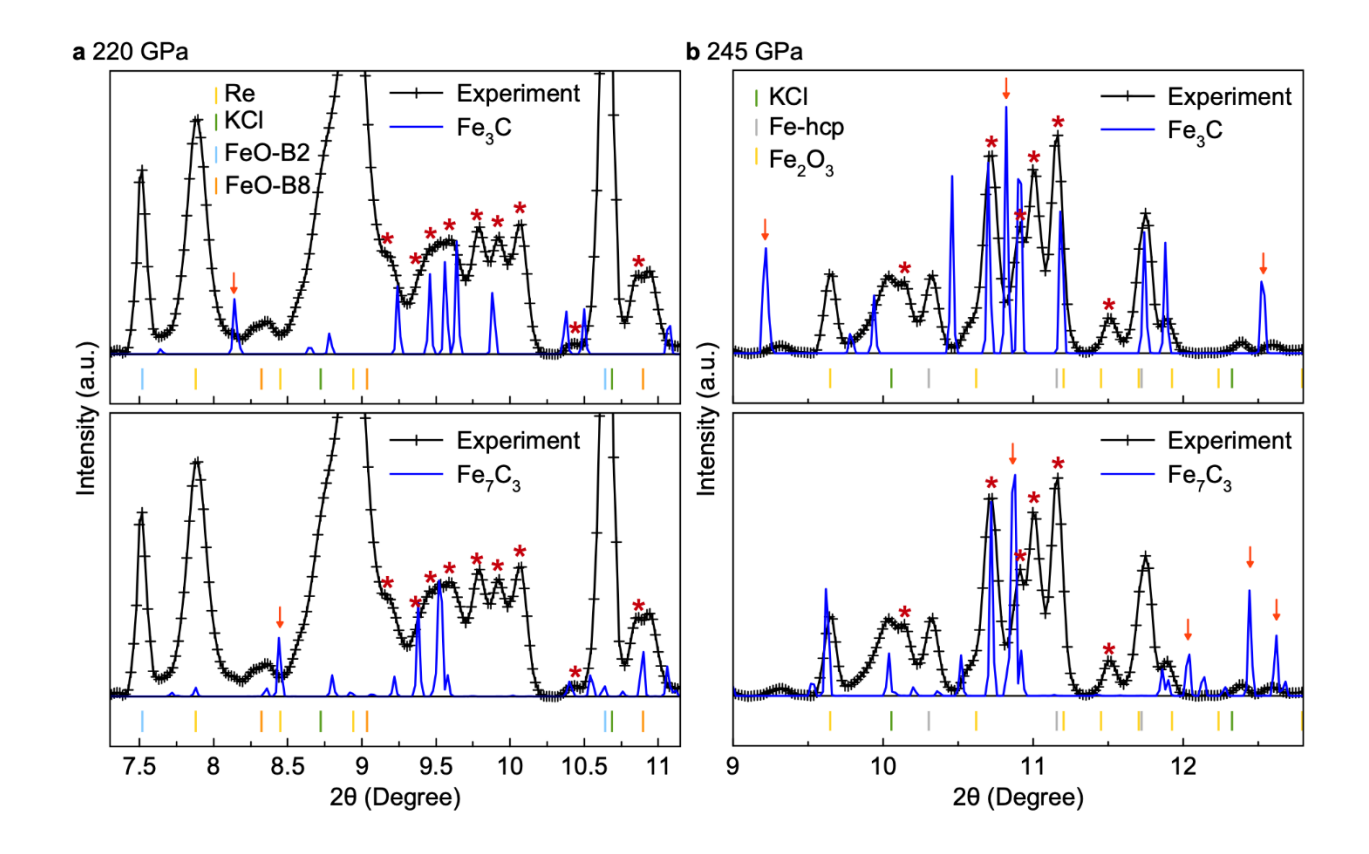


Figure S7 | Comparison between experimental X-ray diffraction patterns and those of Fe₃C/Fe₇C₃. The patterns were collected from (*a*) Fe+FeO reaction at 220 GPa and (*b*) Fe+Fe₂O₃ reaction at 245 GPa. Arrows indicate extra peaks of the Fe₃C/Fe₇C₃ phases. The x-ray wavelength (λ) was 0.2952 Å for the reaction product of Fe and FeO at 220 GPa, and that was 0.3344 Å for the reaction product of Fe and Fe₂O₃ at 245 GPa. The asterisk symbol (*) represents the diffraction peak of the new phases.

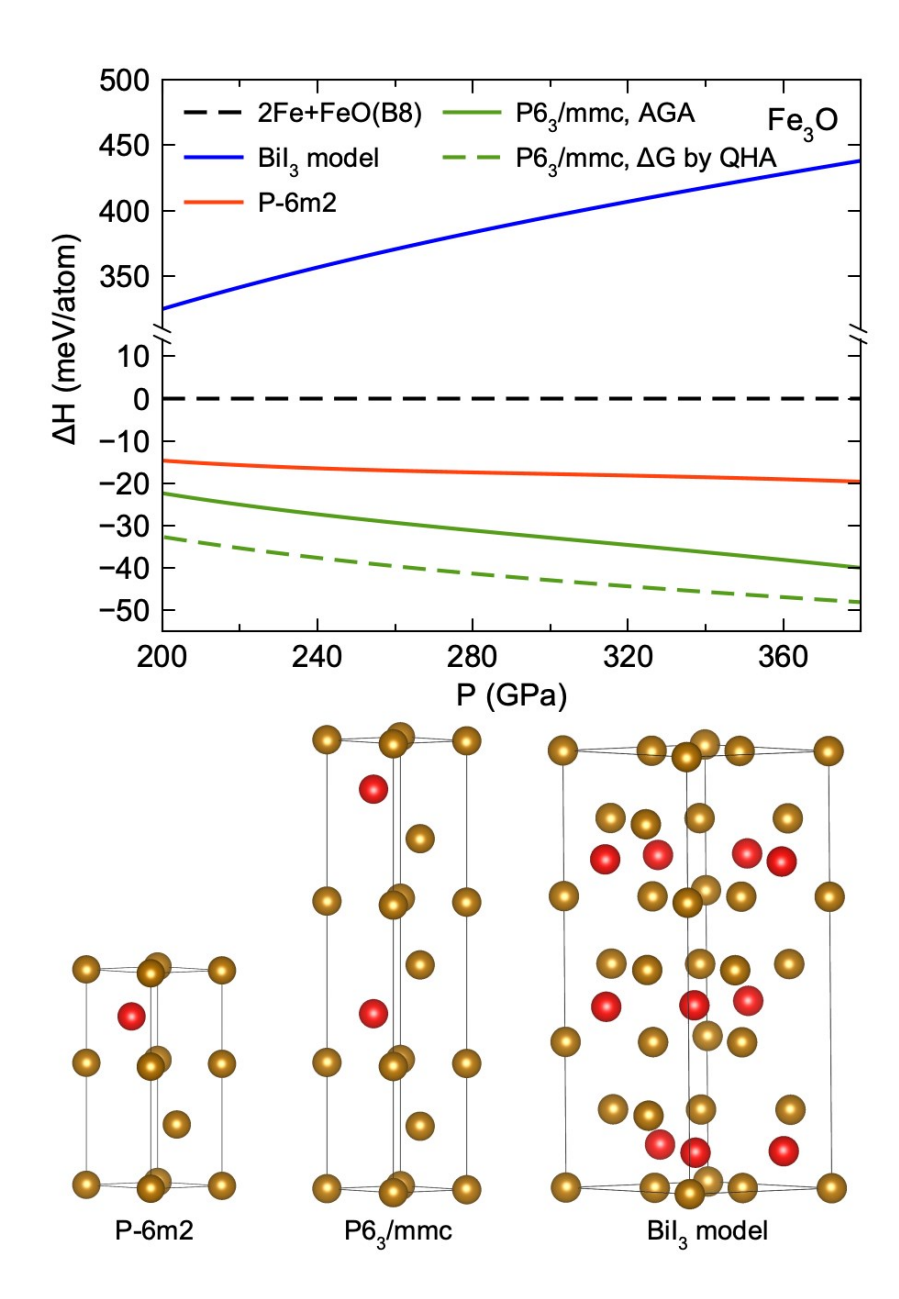


Figure S8 | **Relative enthalpy of Fe₃O models.** The *P*-6*m*2 and BiI₃-type (*R*-3) phases are from Weerasinghe *et al.*¹⁵ and Alfè *et al.*⁶², respectively. The relative enthalpy is referenced to the decomposition products ε-Fe and B8-FeO. The lower panel shows the atomic structures. The FeO-Fe layer stacking in the *P*-6*m*2 phase is ABA while it is ABC in the *P*6₃/*mmc* phase. The dashed line shows the relative Gibbs free energy (ΔG) of *P*6₃/*mmc* phase computed with quasiharmonic approximation (QHA).

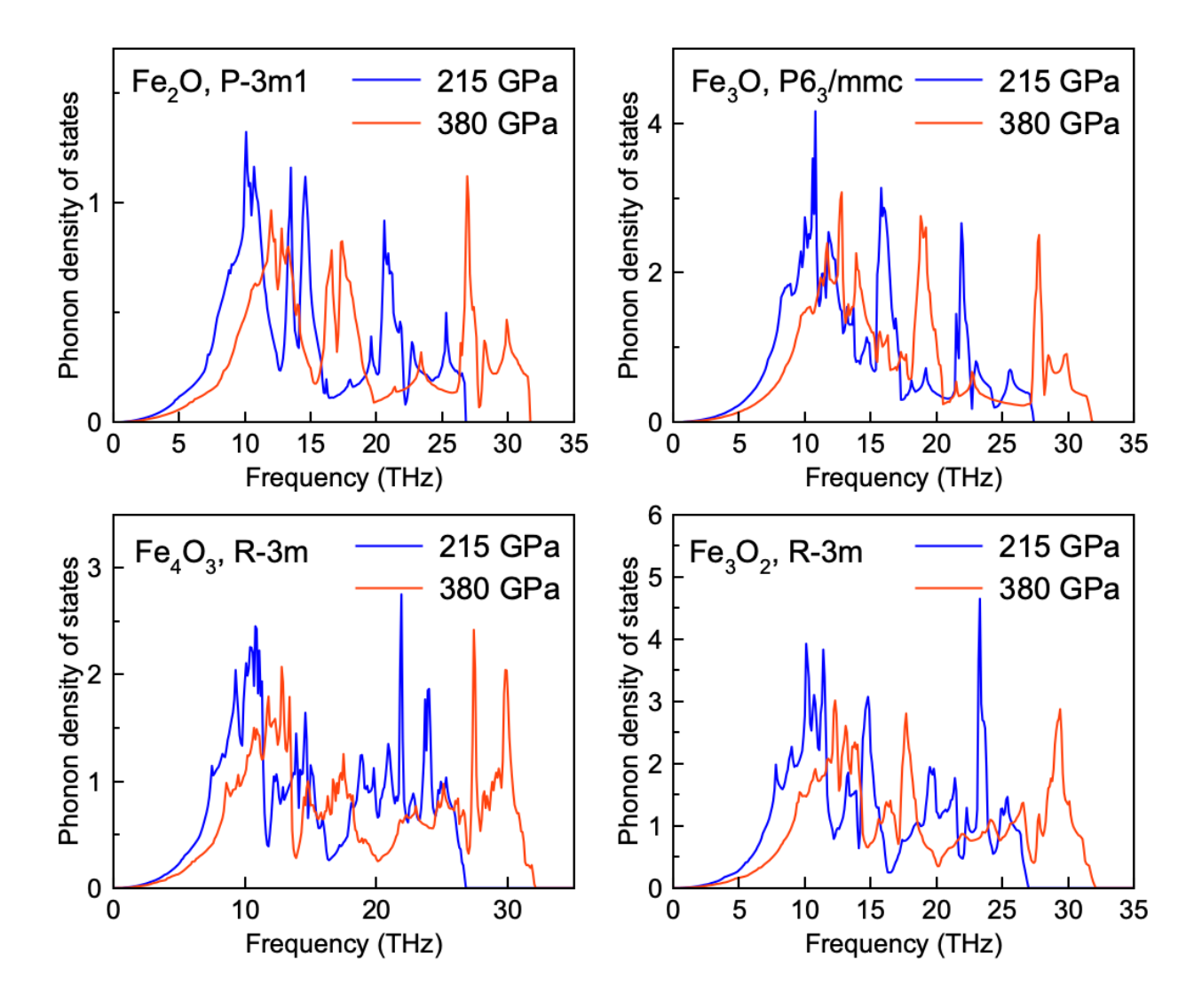


Figure S9 | Phonon density of states of Fe_nO ground state. The absence of imaginary phonon frequencies indicates that all phases are dynamically stable at 215 GPa and 380 GPa.

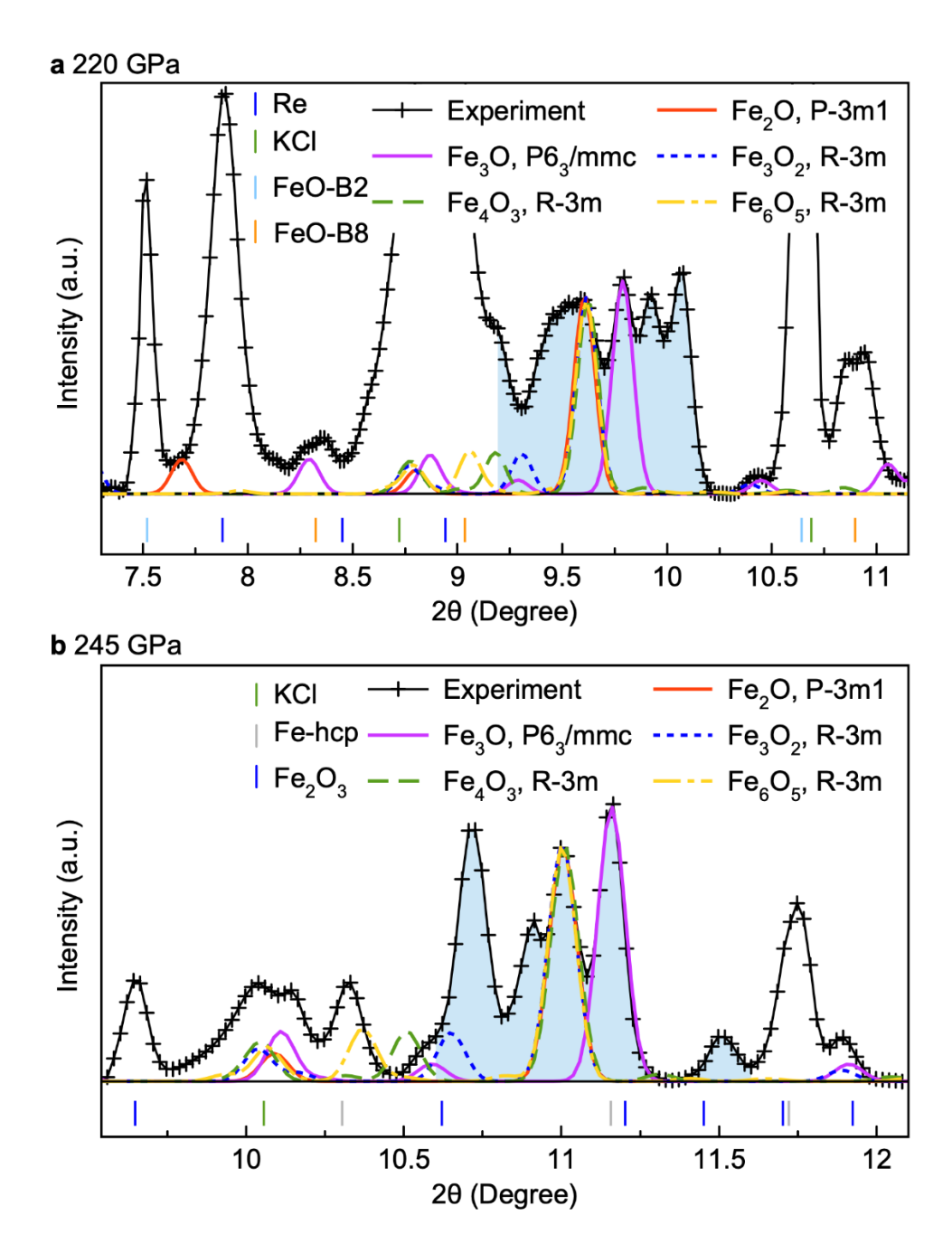


Figure S10 | Comparison between experimental X-ray diffraction patterns and those of the Fe_nO phases in the convex hull found in the AGA searches. The data were collected from (a) Fe+FeO reaction at 220 GPa and (b) Fe+Fe₂O₃ reaction at 245 GPa. The XRD peak positions of starting materials are shown at the bottom.

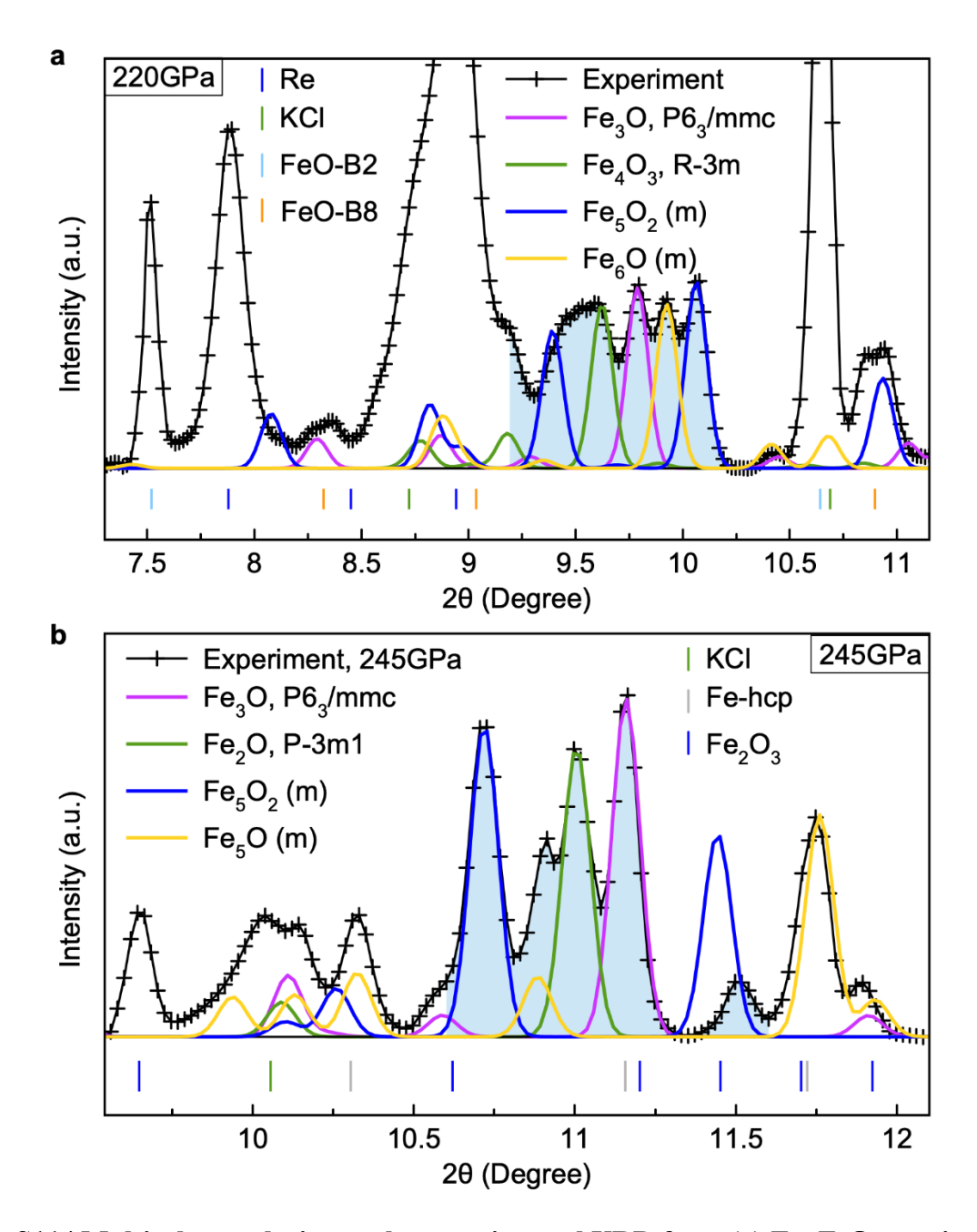


Figure S11 | **Multi-phase solution to the experimental XRD from** (*a*) Fe+FeO reaction at 220 GPa and (*b*) Fe+Fe₂O₃ reaction at 245 GPa. The major unknown peaks in the experimental XRD can be matched by a combination of multiple close-packed Fe-O phases. (*a*) $P6_3/mmc$ Fe₃O and R-3m Fe₄O₃ are ground state phases at 220 GPa while Fe₅O₂ and Fe₆O are metastable phases with 8.0 meV/atom and 4.5 meV/atom above the convex hull, respectively. (*b*) The same Fe₃O and Fe₂O phases are identified at 245 GPa, while Fe₅O₂ and Fe₅O are the metastable phases with 47 and 49 meV/atom above the convex hull, respectively.

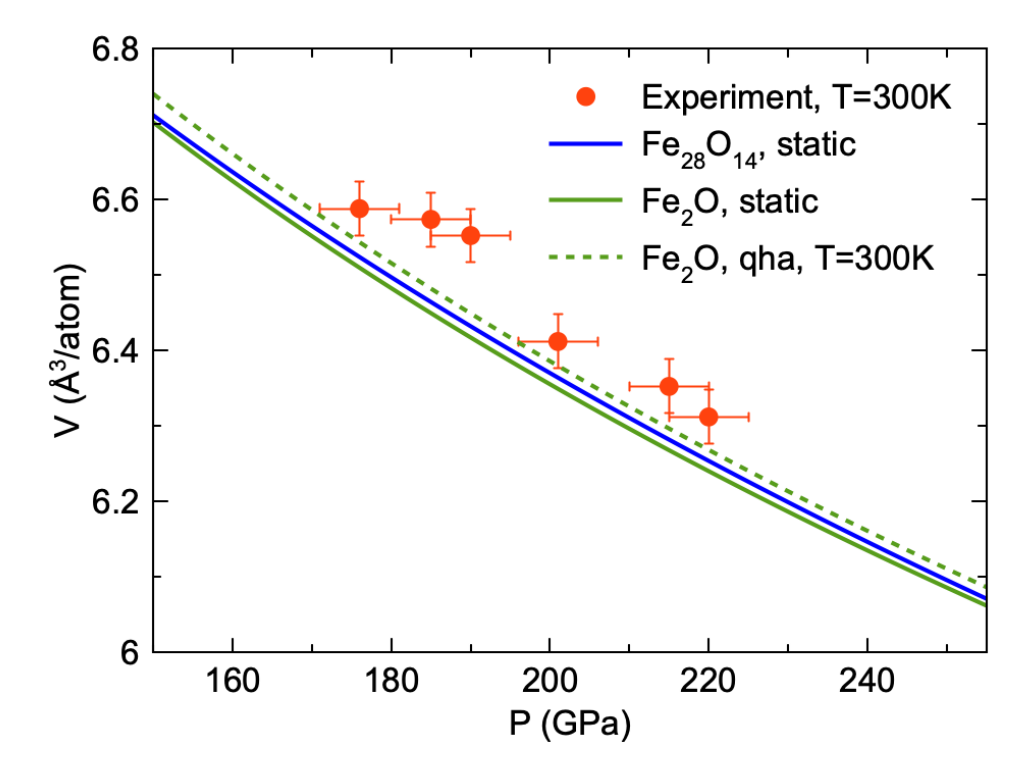


Figure S12 | Experimental compression curve of products from Fe+FeO reaction and theoretical equation of state of the Fe₂₈O₁₄ supercell (blue) and the Fe₂O ground state (P-3m1) (olive). Red symbols represent experimental data from the Fe-FeO reaction product upon decompression at room temperature. The decompression data is limited to ~170 GPa because the x-ray diffraction signal of the new reaction product gradually faded away at pressures less than 200 GPa when the Fe-rich Fe_nO phase entered its unstable pressure field.

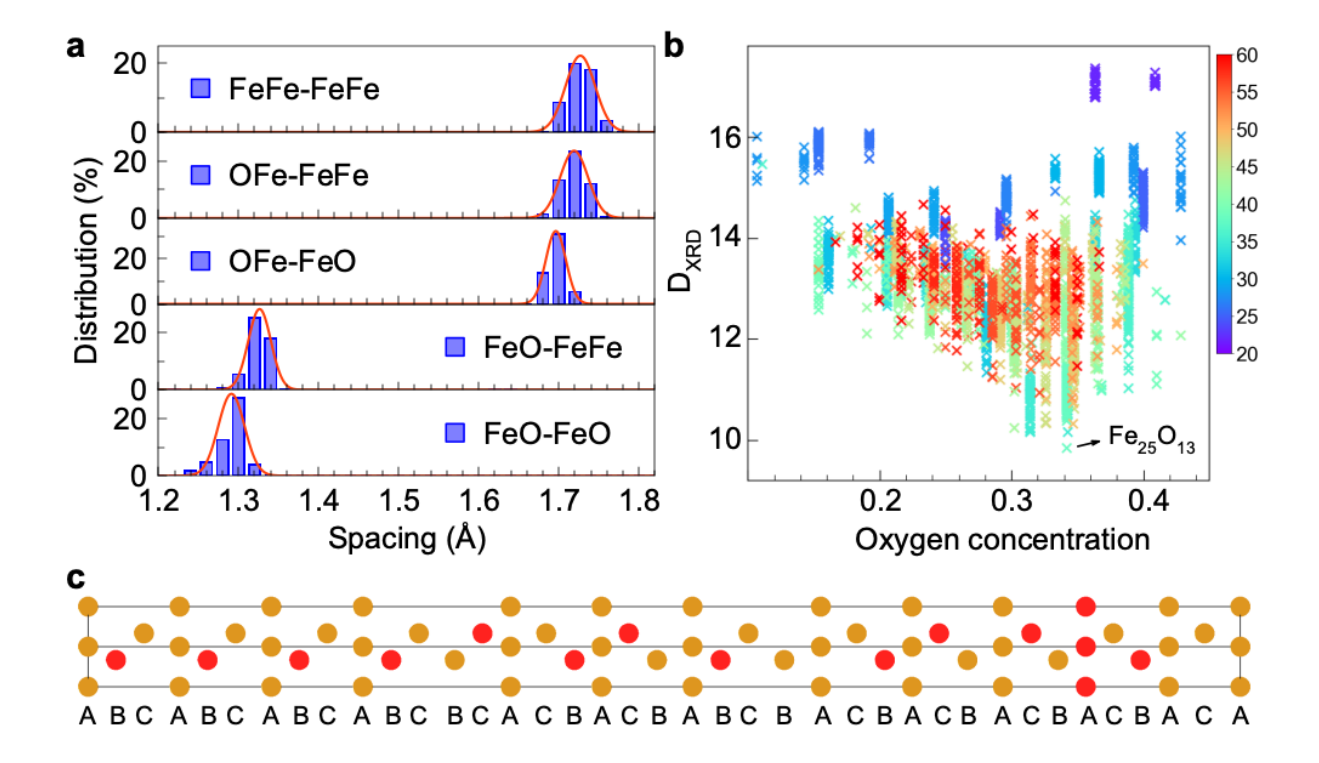


Figure S13 | Reverse Monte Carlo solution for the XRD at 245GPa. (a) Distribution of middle layer spacing in different layer sequences. The red curve is a fitting using a Gaussian distribution. (b) XRD deviation, D_{XRD} , vs. oxygen concentration for various hexagonal supercells resulting from various RMC simulations. Each point represents a final structure achieved by the simulation. Color indicates the number of atoms in the supercell. (c) Supercell structures of Fe₂₅O₁₃. The XRD of Fe₂₅O₁₃ is shown in Fig. 1 of main text.

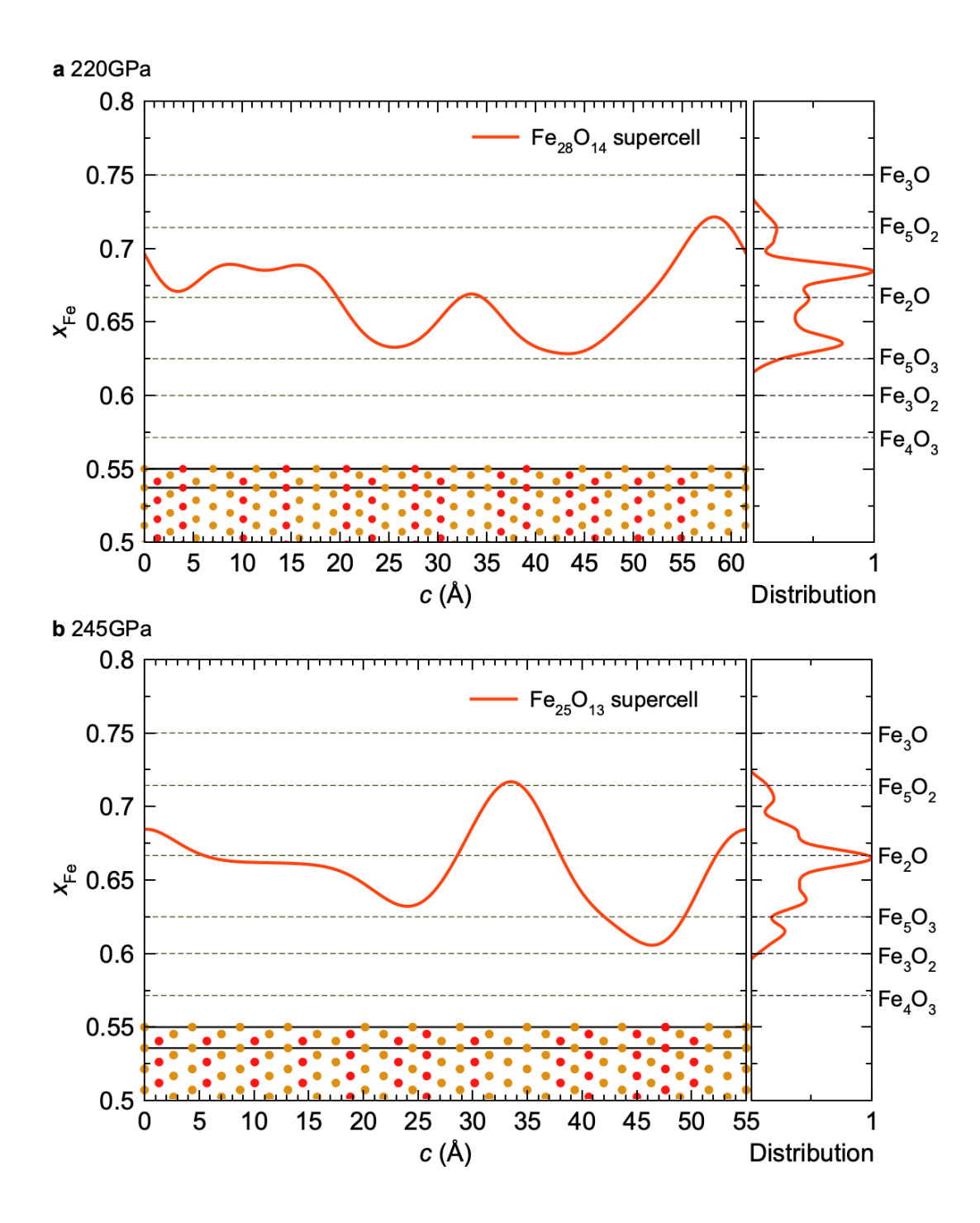


Figure S14 | The profile of Fe composition (x_{Fe}) along the out-of-layer *c-axis* direction. (a) The Fe₂₈O₁₄ supercell identified at 220 GPa and (b) The Fe₂₅O₁₃ supercell identified at 245 GPa. The right panel is the distribution of the Fe local composition.

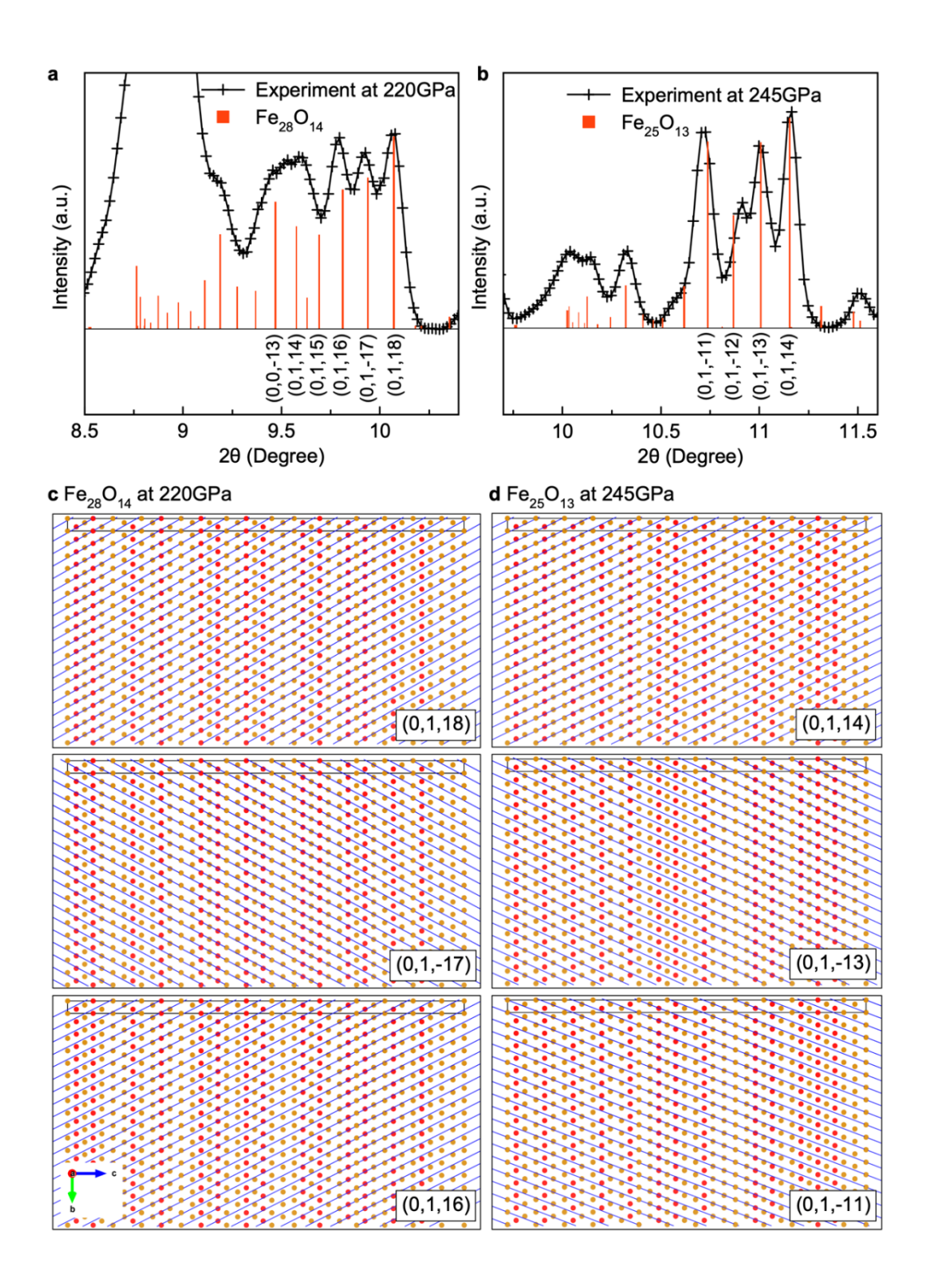


Figure S15 | Miller indices and their corresponding lattice planes of major XRD peaks. (a) and (b) Miller indices of major peaks and (c) and (d) corresponding lattice planes of supercell solutions obtained by RMC simulations at 220 GPa and 245 GPa, respectively.

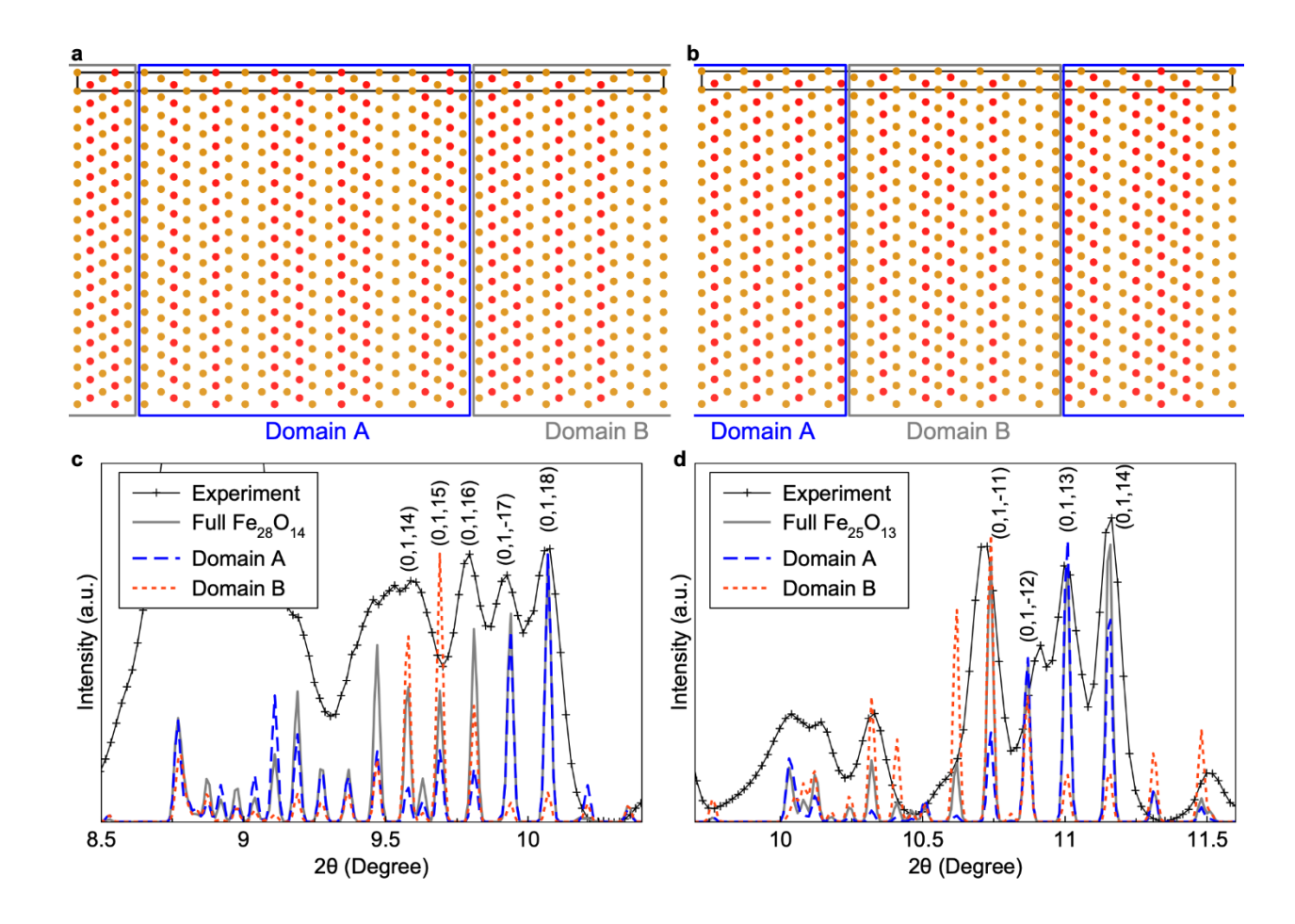


Figure S16 | Domains with different MRO identified in the supercells and their contribution to the XRD. (a) and (b) Domains in the $Fe_{28}O_{14}$ and $Fe_{25}O_{13}$ supercells. (c) and (d) The contribution of different domains to the XRD at 220 GPa and 245 GPa, respectively.

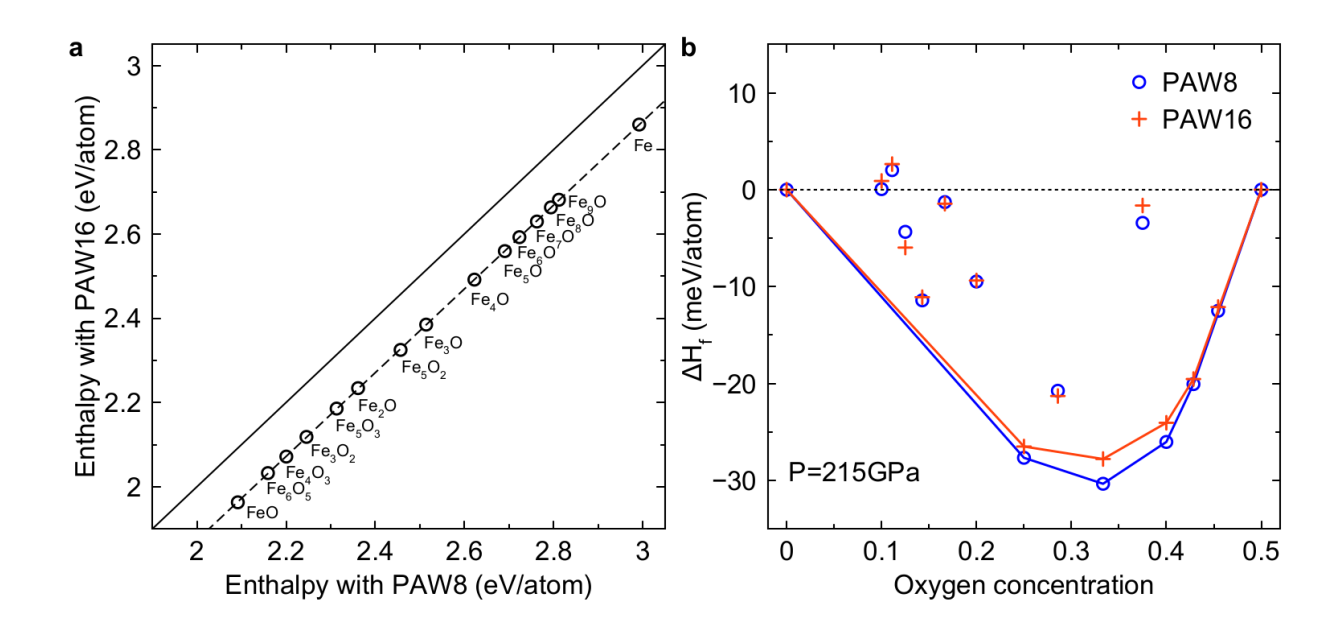


Figure S17 | Comparison between PAW8 and PAW16 potentials. (a) Scatter plot of enthalpies calculations with PAW8 and PAW16 potentials. The structures are the one with lowest enthalpy for each composition. (b) The formation enthalpy is computed using ε -Fe and B8-FeO as reference. Phases in the convex hull are then connected.